

Isotopic production cross sections and recoil velocities of spallation-fission fragments in the reaction $^{238}\text{U}(1\text{A GeV}) + d$

J. Pereira,^{1,*} J. Benlliure,¹ E. Casarejos,¹ P. Armbruster,² M. Bernas,³ A. Boudard,⁴ S. Czajkowski,⁵ T. Enqvist,² R. Legrain,⁴ S. Leray,⁴ B. Mustapha,³ M. Pravikoff,⁵ F. Rejmund,³ K.-H. Schmidt,² C. Stéphan,³ J. Taïeb,³ L. Tassan-Got,³ C. Volant,⁴ and W. Wlazole⁴

¹Universidad de Santiago de Compostela, Santiago de Compostela E-15782, Spain

²Gesellschaft für Schwerionenforschung, Darmstadt D-64291, Germany

³Institute de Physique Nucléaire, Orsay cedex F-91406, France

⁴DAPNIA/SPHN, CEA/Saclay, Gif sur Yvette cedex F-91191, France

⁵CENBG, Gradignan cedex F-33175, France

(Received 2 May 2006; published 8 January 2007)

Fission fragments of 1A GeV ^{238}U nuclei interacting with a deuterium target have been investigated with the Fragment Separator (FRS) at Gesellschaft für Schwerionenforschung (GSI) by measuring their isotopic production cross sections and velocities. Results, along with those obtained recently for spallation-evaporation fragments, provide a comprehensive analysis of the spallation nuclear productions in this reaction. Details about the experimental performance, data reduction and results are presented.

DOI: [10.1103/PhysRevC.75.014602](https://doi.org/10.1103/PhysRevC.75.014602)

PACS number(s): 25.40.Sc, 25.45.-z, 25.85.-w, 29.25.Rm

I. INTRODUCTION

Spallation reactions constitute nowadays one of the most extensively used processes to produce radioactive nuclear beams (RNB) on the entire chart of the nuclides [1]. In addition to their numerous technical and scientific applications (for a review see for instance Refs. [2–6]), this type of reaction has recently turned out to be an optimum tool for investigating the de-excitation of hot nuclei over a wide range of temperatures and fissilities [6–11].

The present article focuses on the experimental study of the spallation-fission fragments produced in the reaction ^{238}U at 1A GeV with deuterium, and constitutes the complementary part of the analysis of spallation-evaporation fragments presented recently by E. Casarejos *et al.* [12]. Both experiments are part of an extensive experimental campaign performed at Gesellschaft für Schwerionenforschung (GSI) to determine the general inventory of nuclear fragments produced in different spallation reactions [6,12–24]. The main goal of the project was the establishment of an extensive benchmark database for the design of accelerator driven systems (ADS) [25,26] and spallation-neutron sources. A restrictive requirement of these applications is the highly precise measurement of the isotopic production cross sections and recoil velocities of spallation fragments.

The challenging performance of this kind of experiments motivated the use of the inverse-kinematics technique, in which the heavy-ion accelerated at relativistic energies collides with a light-nucleus target in such a way that the spallation-reaction products are emitted forward, allowing their analysis with an in-flight magnetic separator. At present, the only laboratory offering the possibility of employing such a technique for studying uranium-induced reactions at relativistic energies

in the GSI [27] in Darmstadt, Germany. Details about this facility, as well as the experimental technique used to separate and identify the reaction products, are presented in the first part of the article. The second part concerns the data analysis performed to evaluate the velocities and isotopic production cross sections of the measured fission fragments. The article ends with a compilation and general discussion of the data. An extensive analysis of these results will be presented in a forthcoming article.

II. EXPERIMENT

A. Experimental setup

In the present experiment, a ^{238}U primary beam was accelerated in the Scherionensynchrotron (SIS) [28,29] up to an energy of 1A GeV. The intensity, of the order of 10^7 ions/s, was continuously measured with the secondary-electron monitor SEETRAM [30,31]. After its extraction, the uranium beam impinged on a cryogenic deuterium target [32] of 201 mg/cm² thickness, isolated from the vacuum line by two titanium foils of 18.16 mg/cm² thickness each. This target was located at 1.69 m from the entrance of the fragment separator (FRS) [33], so that the resulting reaction products were transmitted and measured by the separator before their β decay. A niobium stripper foil of 60 mg/cm² thick was placed downstream of the production target to maximize the fraction of fully stripped fragments.

The FRS is an achromatic zero-degree in-flight separator that consists of four independent stages with their respective image planes (see Fig. 1). The four stages are grouped in two symmetric dispersive areas, so that the entire device remains achromatic. Its high resolving power of 1500, determined for an emittance of 20π mm mrad and a beam spot of 2.7 mm [33], is achieved at the expense of a limited acceptance in magnetic rigidity ($\pm 1.5\%$) and angle (15 mrad around

*Electronic address: pereira@nscl.msu.edu; present address: NSCL/MSU, East Lansing, MI 48824.

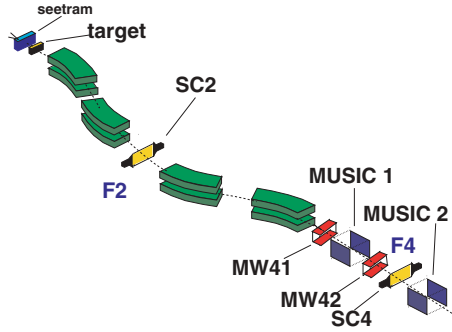


FIG. 1. (Color online) Schematic view of the FRS with its standard detection equipment.

the beam axis). According to the ion optics of the FRS, the separation and identification of the fission fragments was performed by combining the signals measured with the standard detection setup shown in Fig. 1: A pair of plastic scintillators (SC2 and SC4 [34]), placed at the second (F2) and fourth (F4) image planes were used to determine the horizontal (x direction) deflection of the transmitted nuclei and the time-of-flight (TOF) from F2 to F4. Two MUSIC ionization chambers [35], placed at the end of the FRS, provided the energy loss of the nuclei. Finally, two multiwire chambers (MW41 and MW42 [36]) were used to track the transmitted nuclei. All the fast-output signals were filtered by setting the CFD's threshold levels above the electronic noise and the low-amplitude signals generated by light particles. The trigger for the data acquisition was given by the signals from the last plastic scintillator (SC4). A software-defined trigger condition requiring valid position, TOF, angle, and energy-loss signals was used to register valid events.

B. Separation and identification of reaction products by the FRS

1. Separation of transmitted nuclei

The magnetic separation of the nuclides transmitted through the FRS was based on the relationship between the mass-over-charge ratio A/Z of the nuclei, their magnetic rigidity $B\rho$, and the longitudinal component of the relativistic reduced

momentum $\beta\gamma$:

$$B\rho = \left(\frac{A}{Z}\right) \frac{m_0}{e} \beta\gamma, \quad (1)$$

where m_0 the nuclear mass unit and e the electron charge.

For a given nucleus, its magnetic rigidity was determined from the horizontal deflection, measured with the plastic scintillator SC2 at the dispersive image plane, according to:

$$B\rho = (B\rho)_0 \left(1 - \frac{x_2}{D_2}\right), \quad (2)$$

where x_2 is the position of the transmitted nucleus, measured in the dispersive plane F2; D_2 is the dispersion at this image plane, corresponding to the first half of the separator; and $(B\rho)_0$ corresponds to the magnetic rigidity of a nucleus following a central trajectory along the FRS. This latter quantity was determined by multiplying the magnetic fields of each dipole measured with Hall probes with their corresponding curvature radii determined by dividing the calculated magnetic rigidity of the primary beam at 1A GeV by the measured magnetic fields that are necessary to center the beam along the FRS.

The longitudinal component of the reduced momentum $\beta\gamma$ of the transmitted nuclei (or equivalently their longitudinal velocity v) was calculated by dividing the path length l covered by the ions from F2 to F4 by the TOF between the two plastic scintillators SC2 and SC4. To avoid dependences of the velocity on the angle, an angular correction from the tracking detectors MW41 and MW42 had to be included in the path length l .

Together with the mass-over-charge ratio A/Z , we also determined the atomic number of each nuclide to get a full identification. This quantity was deduced from the energy-loss signal ΔE measured with the MUSIC ionization chambers, corrected from the dependencies on the velocity of the transmitted nuclei and on the horizontal positions of the incoming nuclei at the entrance of the detector with respect to the anodes.

The final resolution attained in the separation of the reaction products is illustrated in the left panel of Fig. 2, where the energy-loss signal is plotted against the mass-over-charge ratio for some selected nuclei. The figure was obtained by summing up all the fission settings measured during the experiment.

As far as the selection of transmitted nuclei is concerned, the transversal dimensions of the inner tubes of the FRS and the maximum magnetic dispersion set a limit on the range

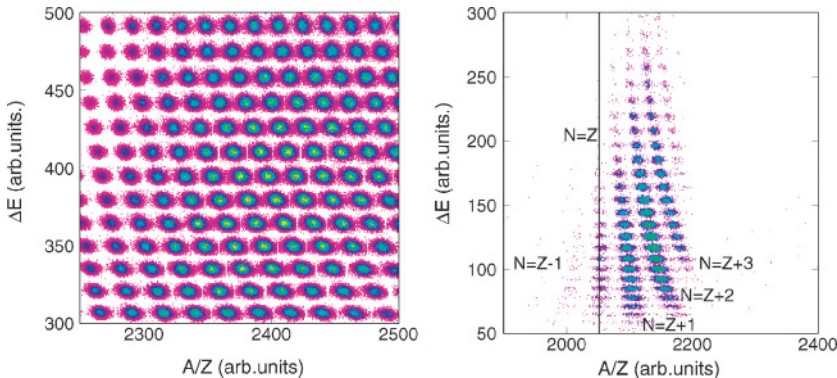


FIG. 2. (Color online) Two-dimensional cluster plots showing the energy-loss signal against the mass-over-charge ratio. (Left) Separated nuclei, represented by the different blobs. (Right) Isospin identification (the vertical line corresponds to nuclei with $N = Z$).

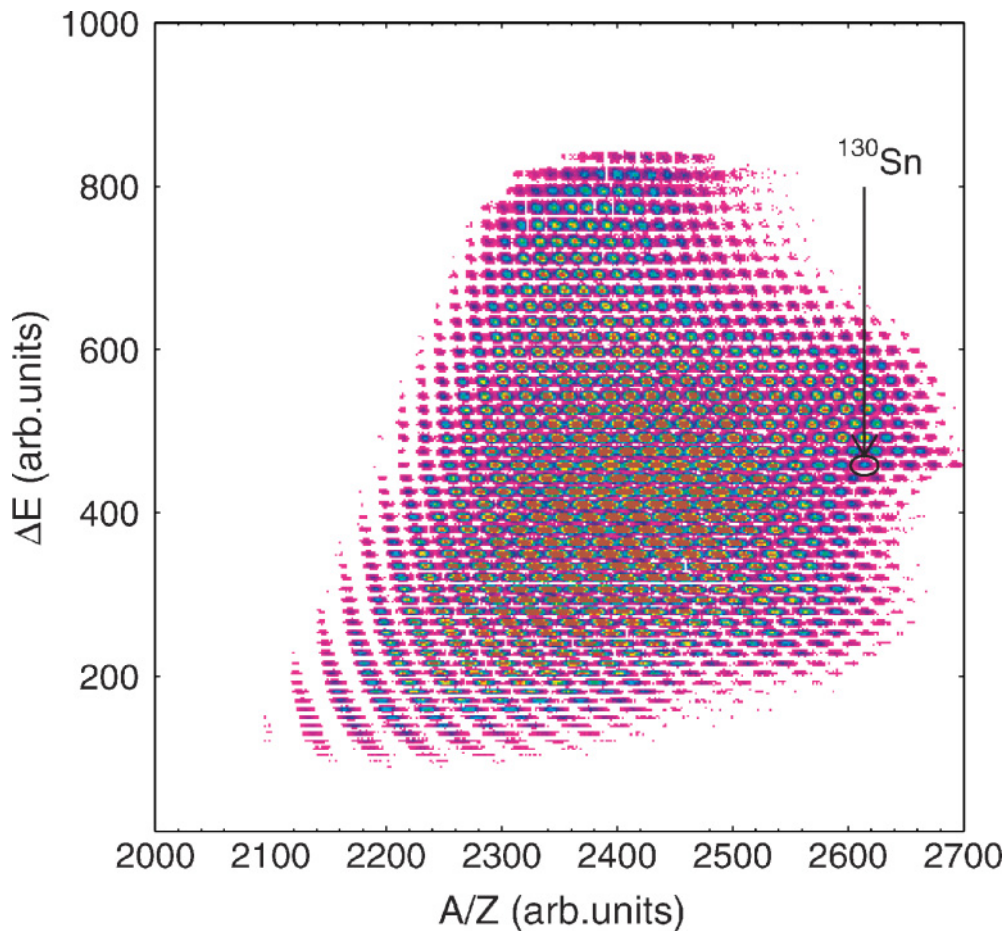


FIG. 3. (Color online) Identification matrix in the form of a scatter plot, showing the energy loss ($\Delta E \propto Z^2$) versus the mass-over-charge of all the nuclei measured in 33 different settings of the reaction $^{238}\text{U}(1\text{A GeV}) + d$. As an example, the fission fragment ^{130}Sn is indicated. The vertical line corresponding to $N = Z$, cannot be seen in the present figure due to the large dynamic color range.

of magnetic rigidities accepted by the separator. Assuming a maximum dispersion of $-6.8\text{ cm}/\%$ at the dispersive image plane, a $B\rho$ acceptance of $\pm 1.5\%$ was deduced from Eq. (2); those nuclei with magnetic rigidities 1.5% greater or lesser than the central value $(B\rho)_0$ were deflected out of the FRS beam line. This limited range of accepted $B\rho$'s, together with the velocity spread, defined a region of A/Z values that could be measured in one single tuning (setting) of the FRS.

Because the nuclei produced in the collision of ^{238}U at 1A GeV with the deuterium target spread out over a wide region of atomic and mass numbers, the FRS had to be adjusted according to the magnetic rigidities of the medium-mass fission fragments to be analyzed. From the calculated values of $B\rho$, a central value $(B\rho)_0$ of the FRS was selected by properly adjusting the magnetic fields of each dipole magnet according to the curvature radii. To cover the region of interest, the measurements were repeated for 33 settings centered on different values of $(B\rho)_0$, separated from each other in steps of 1%.

2. Isotopic identification

The identification of the atomic number Z for each nucleus was deduced using the energy-loss signals ($\Delta E \propto Z^2$) of the ^{238}U beam as a reference.

The identification of mass numbers was obtained from the spectra $(A/Z) \times \Delta E$ (Fig. 2, right): Depending on the values of the mass and atomic numbers of the nucleus, the different nuclei are located at different blobs in this matrix. The possible combinations obtained between the quantities A/Z and Z —where Z and A are integer numbers—define a characteristic pattern in which the nuclei can be grouped within curved lines. The only line with no curvature corresponds to light nuclei with the same number of protons and neutrons ($Z = N$). The next group-line on the right corresponds to nuclei with $N = Z + 1$, which differs a bit from a perfect vertically. If one then goes n steps to the right, the line found corresponds to the group of isotopes with $N = Z + n$. Thus, from the vertical group-line $A = 2Z$ it was possible to identify the mass number of all the nuclides, because their atomic number was well known. The same rule applied to the next lines to the right ($N = Z + 1$, $N = Z + 2$, ...) in such a way that all the nuclei could be identified in mass A and atomic Z numbers.

Figure 3 shows the identification matrix obtained by summing up all the different settings measured during the experiment. From this figure, about 1000 different nuclides could be identified.

III. DATA REDUCTION

A. Determination of recoil velocities

The recoil velocities of the fission fragments were evaluated to investigate the kinematics associated with the reaction mechanism. The spallation reaction itself is characterized by the collision of a heavy uranium projectile with a deuterium target nucleus, followed by the de-excitation of the projectile-like fragments by fission or by evaporation of light particles. The kinematics of the final fragments correspond to the convolution of the velocity distribution produced by the fast collision, and the subsequent de-excitation processes.

In the present experiment, the kinematics of the fission and evaporation fragment productions were separated by measuring the velocity distribution along the beam axis (hereafter referred to as v), filtered by the limited angular acceptance of the FRS. As discussed in Refs. [19,37,38], this limitation truncates the velocity distributions of fission and evaporation fragments in a different manner, in such a way that they could be identified from the resulting measured v distribution. By making use of Eq. (2), it was possible to determine the longitudinal velocities of the nuclei transmitted through the FRS from their positions at the dispersive image plane (F2) and the identified values of Z and A :

$$v = c \left\{ \left[\frac{A/Zm_0c/e}{(B\rho)_0(1 - \frac{x_2}{D_2})} \right]^2 + 1 \right\}^{-1/2}, \quad (3)$$

where c refers to the speed of light. To determine the exact recoil velocities of the reaction products, the values obtained from Eq. (3) had to be corrected by the energy losses of the transmitted nuclei in the different layers of matter situated between the deuterium target and the plastic scintillator at F2 (see Fig. 1). This correction was done by calculating the energy loss of each nucleus along the flight path from the middle of the target—where the reaction was assumed to take place on average—to the second image plane. Finally, the corrected velocities were transformed into the frame of the projectile.

The accuracy of the velocity determined from Eq. (3) was mainly limited by the position resolution of the plastic scintillator SC2, $\Delta x_2 \simeq 2$ mm and the relative resolution of $(B\rho)_0$, of the order of 10^{-4} . These values led to a final relative precision of the velocity of about 3×10^{-4} , which proves to be a real achievement when compared with other experimental techniques.

To reconstruct the v distribution of a given nucleus, the contributions measured in different magnetic settings of the FRS were summed up and normalized to the corresponding beam intensities N_{proj} . As an example of this procedure, Fig. 4 depicts the reconstructed velocity spectra for different nuclei as a function of the mass number in the form of a scatter plot. The upper and lower wings correspond to the transmitted forward- and backward-emitted fission fragments, respectively, whereas the central cloud represents the contribution of evaporation. The separation between the two wings is related to the fission velocity v_{fiss} (defined as the recoil velocity of the fission fragments with respect to the projectile) and its reduction for higher charges can be partially attributed to a

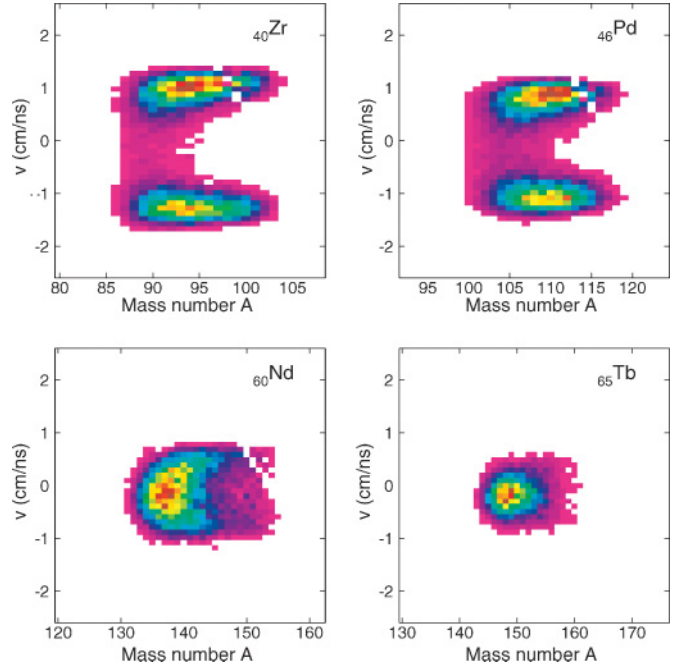


FIG. 4. (Color online) Scatter plots of ${}_{40}\text{Zr}$, ${}_{46}\text{Pd}$, ${}_{60}\text{Nd}$, and ${}_{65}\text{Tb}$ elements showing the velocity distributions measured in the frame of the projectile as a function of the mass number.

decrease in kinetic energy of the two fission partners due to momentum conservation in mass-asymmetric systems and, to a lesser degree, to the weakness of the Coulomb repulsion at large charge asymmetries. Apart from this, the distribution of fragments produced in the two reaction mechanisms is consistent with theoretical expectations: fission fragments are mostly produced with greater neutron excess, whereas evaporation generally leads to nuclei along the so-called evaporation corridor [39], located on the neutron-deficient side of the β -stability valley. Furthermore, as the charge of the element increases, the evaporation contribution is enhanced until it becomes the dominant production mechanism.

The velocities of the fission fragments v_{fiss} in the frame of the projectile were obtained for each isotope by fitting the measured velocity spectra to specific functions that reproduced the contribution from each reaction mechanism. Figure 5 depicts an example of the fit obtained for ${}^{83}\text{Sr}$. The central peak due to the evaporation component was described by a Gaussian function $f_{\text{evap}}(v)$, whereas the forward and backward fission peaks were best reproduced by fitting functions defined by the convolution of a Gaussian and an exponential function. Each of these functions $f_{\text{fiss}}^{\text{f}}(v)$ and $f_{\text{fiss}}^{\text{b}}(v)$ had 4 free parameters, 3 of which corresponded to the Gaussian components, whereas the fourth parameter represented the skewness of the inner tails. The spectra were fitted to a global function $F(v)$ with 11 parameters (3 from the Gaussian evaporation component and 8 from the forward and backward fission fit functions):

$$F(v) = f_{\text{fiss}}^{\text{b}}(v) + f_{\text{evap}}(v) + f_{\text{fiss}}^{\text{f}}(v). \quad (4)$$

The spectra of nuclei produced only by fission or evaporation were well described by the functions of the specific component only.

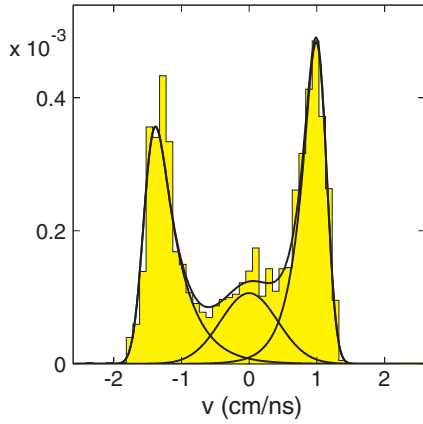


FIG. 5. (Color online) Velocity-spectrum fit for ^{83}Sr showing the contributions from evaporation (central Gaussian curve) and fission (external curves) to the global fit.

As can be seen in Fig. 6, the radius of the spherical fission distribution, corresponding to the velocity of the fission fragments v_{fiss} , could be obtained by halving the distance between the external sides of the forward and backward fission peaks, given by v_f and v_b :

$$v_{\text{fiss}} = \frac{|v_f - v_b|}{2} = \frac{|v_f| + |v_b|}{2}. \quad (5)$$

However, the determination of v_f and v_b from the velocity spectra was quite complicated due to the smooth side tails of the fission peaks.

Alternatively, the values of v_f and v_b could be expressed as a function of the most probable velocities v_f^{max} and v_b^{max} that corresponded to the maximum of the forward and backward

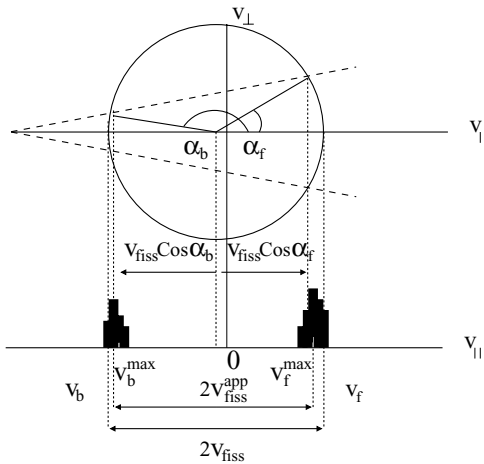


FIG. 6. Schematic representation of the velocity distribution of fission fragments (solid circumference) affected by the cuts produced by the limited angular acceptance of the FRS (dashed lines). The projection of the transmitted nuclei onto the axis parallel to the beam direction (longitudinal component) is shown on the lower part of the figure. The measured most probable forward and backward fission velocities v_f^{max} and v_b^{max} are compared with the real values v_f and v_b . (Note the shift of the velocity distribution with respect to the velocity of the projectile, marked by the origin of the reference frame.)

fitting functions $f_f(v)$ and $f_b(v)$, according to:

$$v_f = v_f^{\text{max}} + \frac{v_{\text{fiss}} - v_{\text{fiss}} \cos \alpha_f}{2} \quad (6)$$

and

$$v_b = v_b^{\text{max}} + \frac{v_{\text{fiss}} + v_{\text{fiss}} \cos \alpha_b}{2}, \quad (7)$$

where α_f and α_b are the forward and backward angles obtained by a Lorentz transformation of the effective FRS angular acceptance α_{eff} (calculated as described in Refs. [37,38]) into the frame of the fissioning system. These two equations can be rewritten as:

$$v_f = v_f^{\text{max}} + v_{\text{fiss}} T_f(v_{\text{fiss}}) \quad (8)$$

and

$$v_b = v_b^{\text{max}} + v_{\text{fiss}} T_b(v_{\text{fiss}}), \quad (9)$$

where $T_f(v_{\text{fiss}}$ and $T_b(v_{\text{fiss}}$ are the v_{fiss} -dependent transmissions of the forward- and backward-emitted fission fragments, calculated according to Refs. [37,38].

The idea behind Eqs. (8) and (9) was that the velocities v_f^{max} and v_b^{max} , obtained from the fitting functions, must be corrected using the fission velocity v_{fiss} and the angular transmission to provide the values v_f and v_b . Because v_{fiss} depends on v_f and v_b [see Eq. (5)], and T_f and T_b on v_{fiss} , we used the recursive algorithm described in Ref. [37] to deduce both the forward and backward transmissions T_f , T_b , and the fission velocity v_{fiss} . The iterative calculation of the algorithm stops when the measured velocities v_f^{max} and v_b^{max} converge to constant values, which are assumed to correspond to v_f and v_b .

There were two sources of uncertainty in the above-described method: first was the determination of v_f^{max} and v_b^{max} from fits and second was the uncertainty of the angular acceptance value α_{eff} used to calculate T_f and T_b . The uncertainties of the former varies considerably from one nucleus to another and depends mainly on the smoothness of the velocity profile; it ranged typically from 1% to 5%, reaching in some particular cases maximum values up to 20%. Concerning the uncertainty due to α_{eff} , it mainly affected the velocities of fragments with rather low transmission. A careful analysis of the ion optics and the geometry of the FRS yielded a total uncertainty for α_{eff} of about 4% [37,38], resulting in an uncertainty in velocity of less than 5%.

Finally, an additional source of error arose from the production of secondary reactions in the deuterium target induced by a heavy primary fission fragment. Such a process would reduce the atomic and mass numbers of the fission fragments, whereas slightly blurring its velocity spectra. As a consequence, the velocity distribution of the isotope can be partially contaminated by the velocities of the heavier fission fragments that underwent a secondary reaction, thus leading to a reduction of the measured values of v_f^{max} and v_b^{max} , as shown in Ref. [19]. This contamination was only significant for the most neutron-deficient fragments.

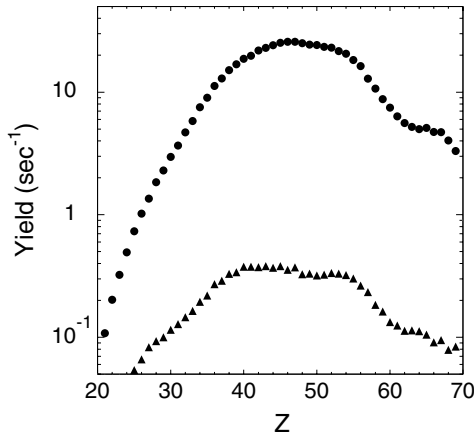


FIG. 7. Element distribution of fission-fragment production yields in the cryogenic deuterium target Y_{tot} (dots) and the titanium dummy target Y_{dummy} (triangles).

B. Determination of production cross sections

In the thin-target approximation, the total production yield of a given isotope is defined by:

$$Y_{\text{tot}}(Z, A) = \frac{N(Z, A)}{N_{\text{proj}}}, \quad (10)$$

where $N(Z, A)$ is the number of nuclei, with a given Z and A , measured during the experiment, and N_{proj} is the number of beam particles. The value of $N(Z, A)$ was obtained by integrating the measured velocity spectra for each nucleus. These spectra were partly contaminated by the fragment production on the titanium windows surrounding the cryogenic deuterium target. To subtract these contaminants, all the measurements were repeated with a titanium dummy target of thickness equivalent to the target windows. The total yields $Y_{\text{tot}}(Z, A)$, integrated over the isotopic chains, are compared in Fig. 7 with the contribution from the titanium dummy target (or equivalently the titanium windows) Y_{dummy} . The production cross sections for the reaction $^{238}\text{U} + d$ were determined from:

$$\sigma_{\text{prod}}(Z, A) = \frac{1}{\chi} [Y_{\text{tot}}(Z, A) - Y_{\text{dummy}}(Z, A)] F, \quad (11)$$

where χ is the density of deuterium nuclei integrated over the target thickness. The factor F includes the different corrections that had to be applied to the measured data due to the limitations of the experimental setup. This factor was calculated according to:

$$F = f_{\text{eff}} f_{\text{sr}} f_{\text{ch}} f_{\text{ev}} f_{\tau}, \quad (12)$$

where f_{eff} accounts for the efficiencies of the experimental setup, f_{sr} corresponds to the corrections that were necessary due to secondary reactions, f_{ch} considers the charge states of the measured nuclei, f_{ev} corrects the contamination from evaporation reactions, and f_{τ} takes into account the dead time of the data acquisition. The calculation of these correction factors has been extensively described in previous analysis of fission- and evaporation-fragment productions (see for instance Refs. [6,13–24]). Consequently, in the present discussion we rather restrict ourself to mention their main features.

The correction due to limitations of the efficiency f_{eff} included the intrinsic efficiency of the detection setup and the angular transmission of the FRS. The former was evaluated for each element by comparing the total number of valid events with the number of events detected with the MUSIC detectors (with an efficiency of 100%). The resulting values were above 98% in most of the cases. The correction due to the limited angular transmission of the FRS was evaluated according to the method described in Refs. [37,38]. This method was based on the calculation of the effective angular acceptance α_{eff} and the analysis of the fission kinematics. The resulting total angular transmission varied largely from values near 100%, for heavy fragments with rather narrow angular emittance, to values around 15%, for the lightest nuclei. The uncertainty associated with this correction method arose from two different sources, namely the calculation of the angular acceptance α_{eff} and the analysis of the kinematics. The final transmission correction error varied significantly from about 2% to 30%, for some particular cases.

Apart from the primary reactions in the target, the beam particles and the reaction products could undergo further reactions in the different layers of matter placed along the FRS, thereby modifying the primary fragment productions. The list of possible “parasitic” targets included the accelerator window, the aluminum SEETRAM foils, a niobium stripper foil behind the target, and the plastic scintillator SC2. The probability for a given nucleus to undergo a secondary reaction was estimated by multiplying the production cross sections, obtained from Glauber-type model calculations [40,42], by the number of impinging beam particles and the number of target nuclei of the corresponding layer of matter. Most of the fragments produced in the aluminum SEETRAM foils and the accelerator window were not transmitted through the FRS due to their large distance with respect to the entrance of the separator that reduced significantly the value of α_{eff} . Moreover, since these contaminating targets were also present in the settings with the titanium dummy target, their contribution to the production cross sections were already subtracted according to Eq. (11). The correction due to secondary reactions induced in the niobium foil and the plastic scintillator SC2 reached rather low values ranging from 10%, for the lightest elements to almost 20% for the heaviest.

Furthermore, the primary fragments produced in the reaction $^{238}\text{U}(1A \text{ GeV}) + d$ could undergo a secondary reaction before leaving the rather thick deuterium target. These secondary products could also induce a ternary reaction resulting in a multistep reaction chain. The multiple reaction contaminants did not spread uniformly over the total fragment production but concentrated in some specific regions close to the evaporation corridor. In the case of fission fragments, this contamination mainly affected the neutron-deficient isotopes, gradually increasing as the neutron number decreases. In the present analysis, we used the correction method proposed by P. Napolitani *et al.* [43]. According to these authors, the measured productions (referred to as apparent cross sections $\bar{\sigma}$) were formulated through a system of master equations that included the losses of fragments due to their interaction in the target and the gains due to the contamination from intermediate multiple reactions. A detailed discussion of this

model and the underlying approximations used to solve the set of master equations can be found in Ref. [43]. For each element, the correction factor was found to be constant within 5% to 7% for most of the isotopes and to drastically drop down when approaching the neutron-deficient side, wherein the corrections reached values close to 100%.

In addition to secondary nuclear reactions, the residual nuclei could also pick up or strip off some electrons due to the atomic interactions with the different layers of matter. The corresponding fraction of bare ions was maximized by placing a niobium stripper foil of 60 mg/cm² thickness behind the target. However, the charge-state configuration of the transmitted ions could change from the first to the second stage of the FRS due to the interactions with the plastic scintillator SC2. As explained in Ref. [44], the strong correlation between the charge state of the transmitted ions and their transversal positions at the final image plane makes it possible to discriminate any charge-state change along the FRS. To avoid ambiguities in the charge identification, we restricted the present analysis to ions with the same charge-state configuration in both stages. According to this criterion, the losses of measured nuclei that were not fully stripped in the two stages of the FRS had to be corrected. For each isotope, a correction factor f_{ch} —which is the product of the fractions of bare ions behind the niobium stripper foil (first stage) and behind the scintillator SC2 (second stage)—was determined. Each fraction being the inverse of the probability of the fully stripped ions in the FRS can be calculated using the GLOBAL code [45,46]. The resulting correction factors are below 10% for the range of elements analyzed in the present work.

Regarding the correction due to the dead time of the data acquisition f_{τ} , the total number of physical triggers generated by the logic of the experiment and the number of events processed by the data acquisition were counted for each setting with scalers. The ratio between both numbers provided the value of the dead time, which was around 15% for most of the settings. Furthermore, the intensity of the primary beam was checked continuously to keep the dead time below 30%.

Finally, because the aim of the present work was the determination of the production cross sections of fission fragments, we had to disentangle the evaporation-reaction contributions to the measured cross sections. By comparing the productions of all the fragments produced in the cryogenic deuterium target and the titanium dummy target we saw that the evaporation fragments measured in the former system were mainly produced in the titanium windows. However, after subtracting these contaminants, a small evaporation component was still observed in the reaction $^{238}\text{U}(1\text{A GeV}) + d$ for heavy neutron-deficient fission isotopes. In a former analysis of spallation-evaporation fragments produced in this reaction [12], it was found that these nuclei populated the evaporation corridor situated on the neutron-deficient side of the chart of the nuclides [39], from uranium isotopes down to elements with atomic numbers about $Z = 58$. Below this value, the evaporation component dropped quickly—though still contributing to the production of the most neutron-deficient isotopes—whereas the fission production increased very fast, particularly in the neutron-rich side. Therefore, we

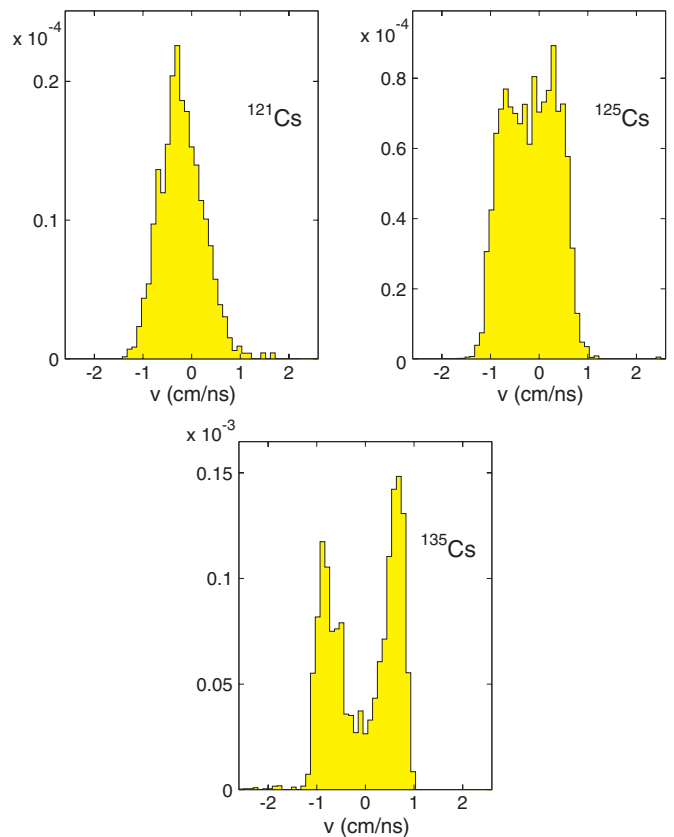


FIG. 8. (Color online) Measured velocity spectra of three cesium isotopes measured in the reaction $^{238}\text{U}(1\text{A GeV}) + d$.

expected both reaction mechanisms to coexist in the region of light evaporation nuclei and heavy fission fragments, with a transition from evaporation to fission as the neutron number increases. Figure 8 illustrates this trend by showing the velocity spectra of three different cesium ($Z = 55$) isotopes. The lightest and heaviest isotopes were mainly produced by evaporation and fission, respectively, whereas an intermediate situation was found for ^{125}Cs , wherein a weak evaporation component was strongly mixed with the dominant fission mechanism (see also Ref. [12]).

The evaporation contamination to the measured fission fragments was estimated using a phenomenological model based on the two-step formalism [47]. A Glauber-type Monte Carlo subroutine [41] was chosen to reproduce the fast interaction between the projectile and target. The evaporation stage was simulated with the statistical de-excitation ABLA code [10,42] and the PROFIL fission mass-distribution subroutine [48]. Details of these codes are well beyond the scope of the present article; it is sufficient to mention here that the reliability of the calculations in estimating evaporation productions in the region of neutron-deficient heavy nuclei was verified by comparing the results with the evaporation cross sections measured for some nuclei. Our estimations agreed with the experimental results within the precision requirements of the present analysis. Furthermore, the separation method discussed in Ref. [12] was used in the present analysis for some nuclei and compared with the technique described above. Both methods agreed within their respective uncertainties, thus

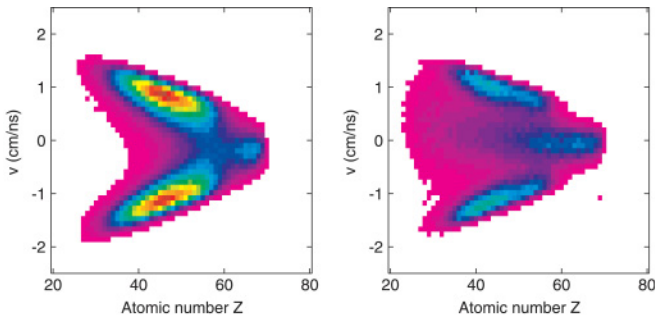


FIG. 9. (Color online) Velocity distributions as a function of the atomic number of fragments measured with the deuterium target enclosed in the titanium container (left) and with the titanium dummy target (right).

demonstrating their capabilities to disentangle the two reaction mechanisms.

IV. RESULTS

A. Velocities of fission fragments

Figure 9 shows the velocity distributions of the fission fragments (in the projectile frame) measured in the reaction induced in the deuterium target surrounded by the titanium windows (left) and in the titanium dummy target (right). The distributions were obtained for each element by integrating the contributions of the whole isotopic chain. In the figure, the evaporation fragments lay in a region of velocities close to that of the primary beam, whereas the forward- and backward-emitted fission fragments correspond to the upper and lower wings. The increase of the fission velocities as the atomic number of the fragments decreases is a natural consequence of momentum conservation between the light and heavy fission fragments in the frame of the fissioning system.

The velocities v_{fiss} of the fission fragments with atomic numbers ranging from $Z = 23$ to $Z = 66$ were determined according to the method described in Sec. III. Figures 10–12 show the isotopic chains of these velocities v_{fiss} for all the measured fragments. The numerical values, with their associated uncertainties are included in Tables I–IV.

As a general trend, one observes a general reduction of the average fission velocities as the charge of the fission fragments increases. This trend is explained by momentum conservation of the two fission partners: After scission, the total kinetic energy of the system (i.e., the sum of the kinetic energies of each fission partner) comes almost entirely from the Coulomb repulsion between the two nascent fragments. Due to momentum conservation, the lightest nucleus will acquire more velocity than the heavier one, thus explaining the results shown in the figures.

Regarding the trends observed for a given element, the velocities reach a maximum value for the most neutron-rich isotopes, then evolve through a plateau for less neutron-rich nuclei and finally decrease in the most neutron deficient side, with an abrupt decline of v_{fiss} to values 20% below the maximum. The characteristic pattern shown in these figures was already observed in the analysis of fission fragments produced in

the reaction $^{238}\text{U}(1\text{A GeV}) + p$ [19]. According to this work, the abrupt decrease of the velocities in the neutron-deficient side can be attributed, to some extent, to the contamination of secondary reactions from primary fission fragments. As discussed above, to estimate such an effect, we have used the model proposed by P. Napolitani *et al.* [43]. Those nuclei with a secondary-reaction component greater than 50% are represented in Figs. 10–12 by empty dots. As expected, they correspond to the most neutron-deficient isotopes.

To understand the observed isotopic dependence of the velocities, a comparison between the values measured in the present experiment and those obtained from the scission-model developed by Wilkins *et al.* [49] is shown in Figs. 10–12. The different lines drawn on top of the experimental values correspond to velocities acquired by fission isotopes coming from different fissioning systems. Surprisingly, the distribution of these systems extends over a rather wide range of elements: The most neutron-rich isotopes stem from the heaviest fissioning elements, including uranium, whereas the neutron-deficient ones are populated by lighter fissioning systems like mercury. This trend is in agreement with the $Z_{\text{fiss}}^2/A_{\text{fiss}}$ dependence of the fissility: As a consequence of the low fissilities of light parent nuclei (low Z_{fiss}), only the most neutron-deficient isotopes (low A_{fiss}) have a chance for undergoing fission due to their smaller fission barriers; the residues produced by these parent nuclei populate thus the neutron-deficient side. On the contrary, the high fissilities of heavy fissioning systems are rather insensitive to a variation of the neutron number, thus extending their productions to more neutron-rich nuclei. A detailed analysis of these results will be discussed in a forthcoming paper.

B. Isotopic production cross sections of fission fragments

The production cross sections of 939 fission fragments measured in the present work are represented as a scatter plot on top of the chart of the nuclides in Fig. 13 (see also Tables V–IX). They cover a region on the neutron-rich side of the valley of stability, with elements ranging from vanadium ($Z = 23$) to thulium ($Z = 69$). The most populated region corresponds to elements between niobium ($Z = 41$) and cadmium ($Z = 48$) with decreasing intensities for lower and higher atomic numbers. For most of these elements, the maximum productions span an extended flat ridge shifted by 2–3 mass units to the right side of the valley of stability. Above the doubly closed shell $Z = 50$ $N = 82$, an enhanced fission-fragment production is observed on the neutron-rich side.

Figures 14–16 provide a more detailed survey of the fission-fragment production, showing the isotopic production cross sections for all measured fission fragments. The measured cross sections range from about 30 mb for intermediate masses of the different elements down to values as low as $2 \mu\text{b}$ on the neutron-rich side.

As a general trend, the isotopic chains of the fission fragments follow a wide Gaussian distribution with mean neutron numbers slightly shifted toward the neutron-rich side of the valley of stability. The maximum production covers an

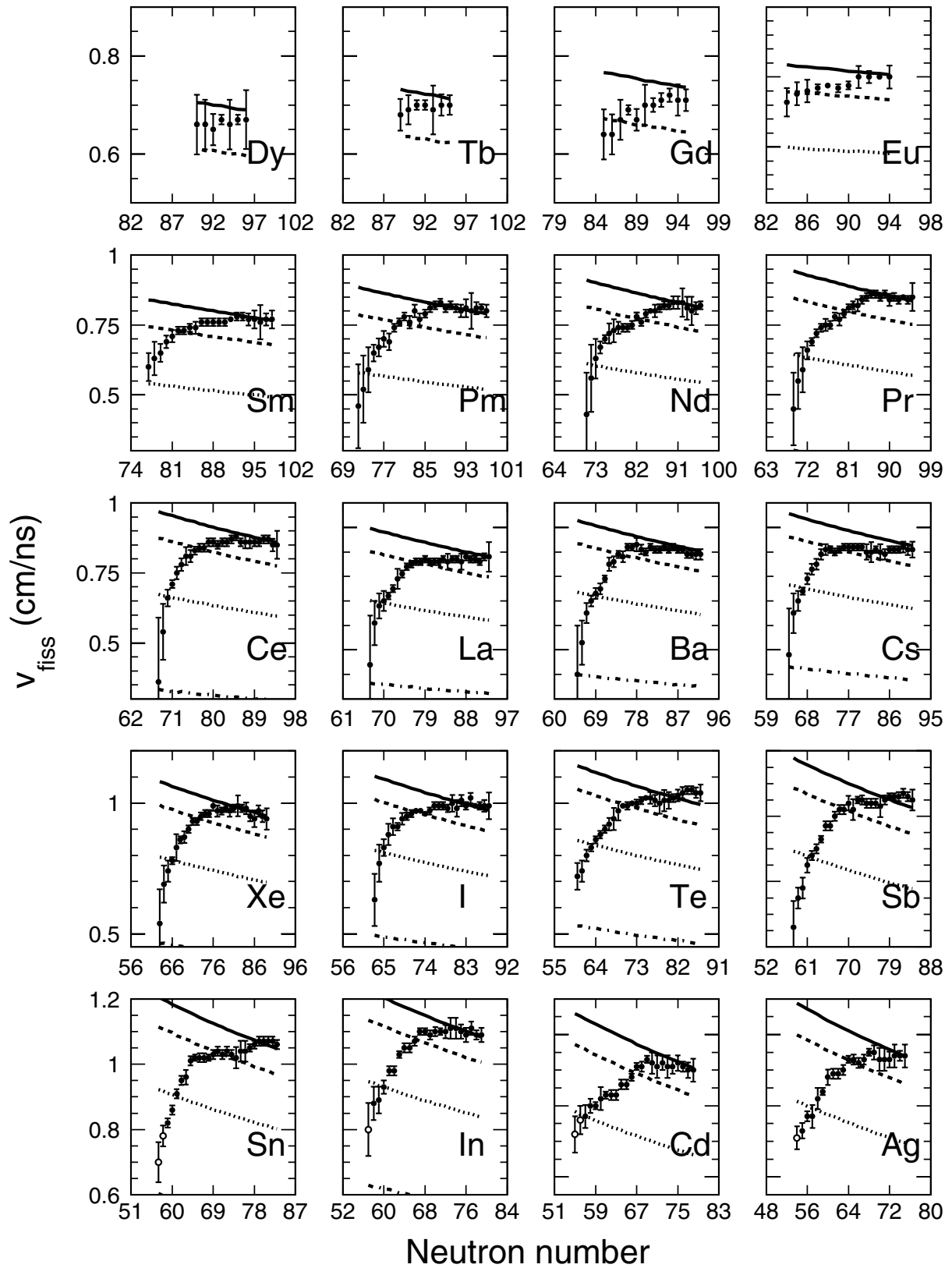


FIG. 10. Isotopic distribution of velocities of fission fragments in the range $23 \leq Z \leq 66$, produced in $^{238}\text{U}(1\text{A GeV}) + d$ (dots) compared to the values calculated with the scission model [47] (see text for details). The calculations were obtained for different fissioning systems: uranium $Z = 92$ (solid line), radium $Z = 88$ (dashed line), mercury $Z = 80$ (dotted line), and rhenium $Z = 75$ (dash-dotted line). Empty dots correspond to nuclei with a secondary-reaction contamination greater than 50%. (Total errors are shown when larger than symbols.)

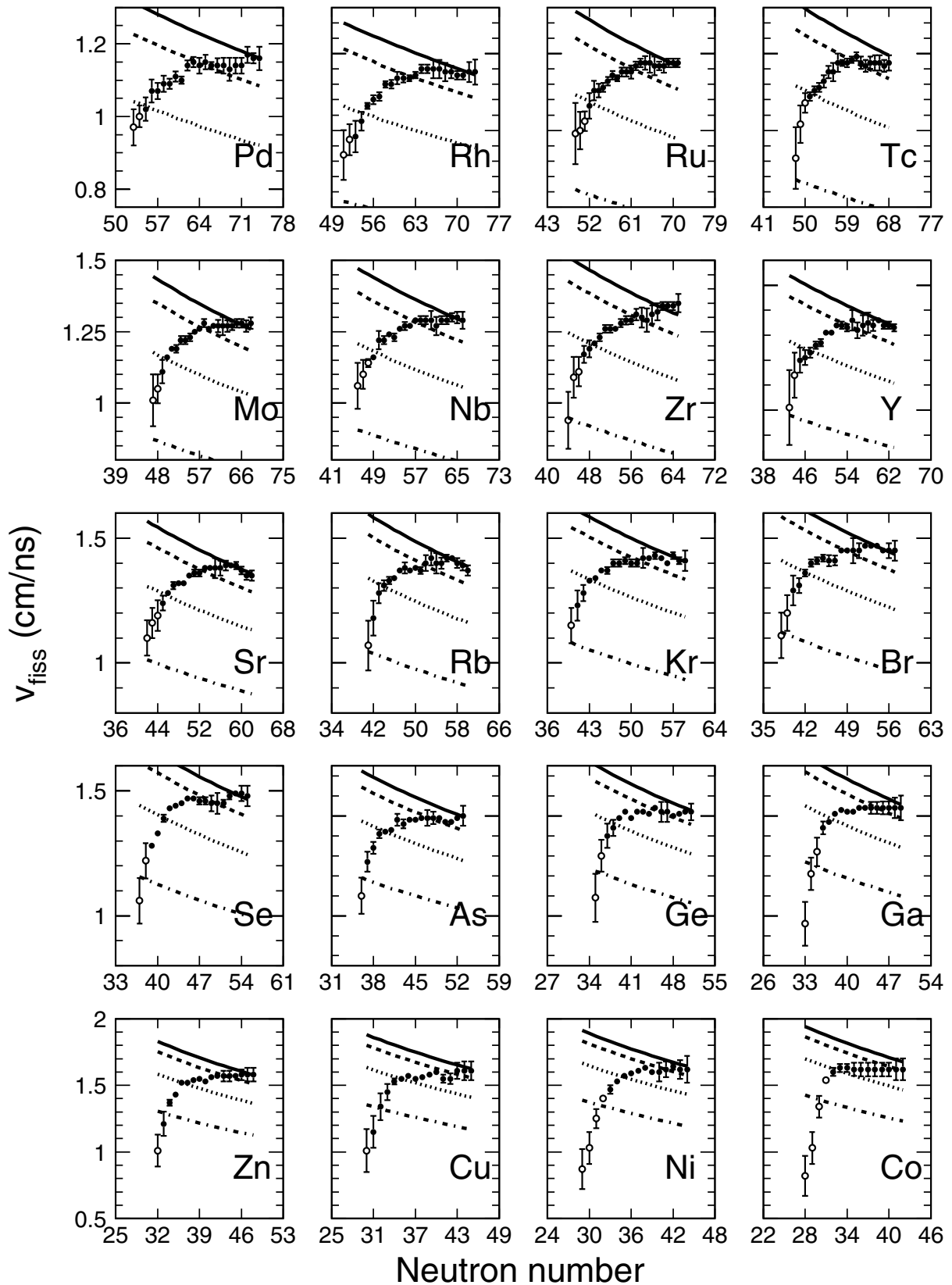


FIG. 11. Isotopic distribution of velocities of fission fragments in the range $23 \leq Z \leq 66$, produced in $^{238}\text{U}(1A \text{ GeV}) + d$ (dots) compared to the values calculated with the scission model [49] (see text for details). The calculations were obtained for different fissioning systems: uranium $Z = 92$ (solid line), radium $Z = 88$ (dashed line), mercury $Z = 80$ (dotted line), and rhenium $Z = 75$ (dash-dotted line). Empty dots correspond to nuclei with a secondary-reaction contamination greater than 50%. (Total errors are shown when larger than symbols.)

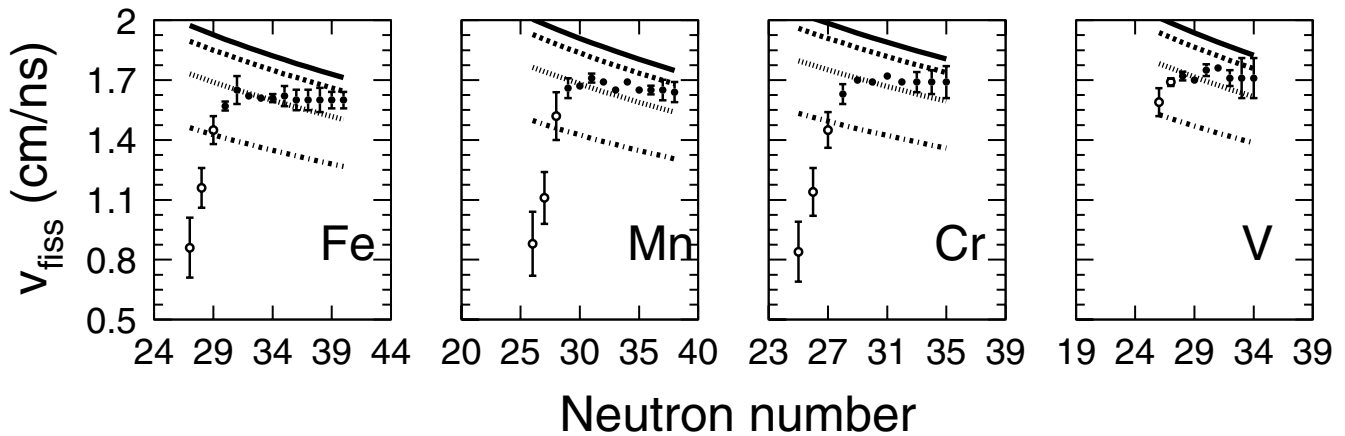


FIG. 12. Isotopic distribution of velocities of fission fragments in the range $23 \leq Z \leq 66$, produced in $^{238}\text{U}(1\text{A GeV}) + d$ (dots) compared to the values calculated with the scission model [49] (see text for details). The calculations were obtained for different fissioning systems: uranium $Z = 92$ (solid line), radium $Z = 88$ (dashed line), mercury $Z = 80$ (dotted line), and rhenium $Z = 75$ (dash-dotted line). Empty dots correspond to nuclei with a secondary-reaction contamination greater than 50%. (Total errors are shown when larger than symbols.)

extended region of elements around ^{46}Pd , which corresponds to symmetric fission. For some elements above $Z = 50$, these Gaussian shapes display a pronounced shoulder on the neutron-rich side related to the contribution of the asymmetric fission channels Standard I (SI) and Standard II (SII) [49–51] (with maximum fission productions at $N \simeq 82$ and $N \simeq 88$, correspondingly) from low-energy fission of nuclei close to ^{238}U . The polarization of the heavy asymmetric fission fragments toward the neutron-rich side, makes the lighter asymmetric partners to move toward the valley of stability, leading to a less pronounced shoulder near the maximum of the isotopic chains, as shown for elements between ^{33}As and ^{42}Mo . This double-humped structure is not observed for elements above ^{59}Pr and below ^{30}Zn .

The total fission cross section, obtained by summing up all the individual isotopic production cross sections was found to be $(2.00 \pm 0.42 \text{ b})$. To account for the isotopes that were

not measured, we extrapolated the isotopic chains shown in Figs. 14–16. The contribution from the missing fragments to the total fission cross section was found to be negligible compared with the total uncertainty. At the present moment, fission data of uranium on deuterium are scarcely represented in the current available databases. After a systematic literature search on the EXFOR [52] database, the only measurements found corresponded to deuteron-induced fission of uranium at energies below 200 MeV [53]. A comparison of these data with our results was possible by extrapolating the former according to the systematics of Prokofiev [54] for proton-induced fission reactions. In doing so, we had to consider the two main differences between proton and deuteron reactions at these energies, namely the twice-larger average energy introduced by deuterons with respect to protons, due to their additional nucleon, and the higher total reaction cross section with respect to protons. Thus, the total fission cross section measured by Stevenson *et al.* [53] at 190 MeV for deuteron-induced reactions on uranium ($2.49 \pm 0.05 \text{ b}$) was compared to the value given by Prokofiev at $2 \times 190 \text{ MeV} = 380 \text{ MeV}$ for protons (1.44 b). The differences between these data were entirely attributed to the higher total reaction cross section for deuterium, leading to a scaling factor of $S = 2.49/1.44 = 1.73$. To extrapolate the value of Stevenson measured at 190 MeV to 1 GeV, we multiplied the cross section calculated by Prokofiev at 2 GeV (1.18 b) by the factor S , which yields 2.04 b. This value compares very well with our result.

The total reaction cross sections could be determined by adding the total evaporation cross section of $(0.91 \pm 0.11 \text{ b})$ obtained by E. Casarejos [12] for the reaction $^{238}\text{U}(1\text{A GeV}) + d$, to the total fission cross section measured in the present work. The resulting value of $(2.91 \pm 0.43 \text{ b})$ is still compatible with the 2.51 b calculated with the Glauber-type model of P. J. Karol [40], which assumes a Gaussian density profile with $r(\text{rms}) = 2.1 \text{ fm}$ for the deuteron nuclei [55].

In contrast to other existing experimental techniques, the total fission cross section obtained in the present work was

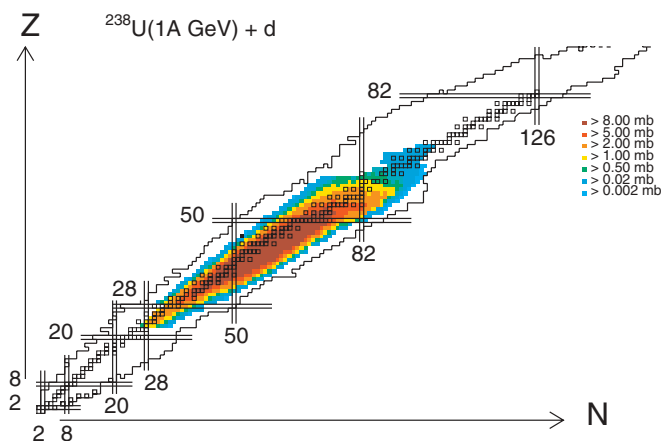


FIG. 13. (Color online) Measured isotopic production cross sections of fission fragments in the reaction $^{238}\text{U} + d$ at 1A GeV on top of the chart of the nuclides.

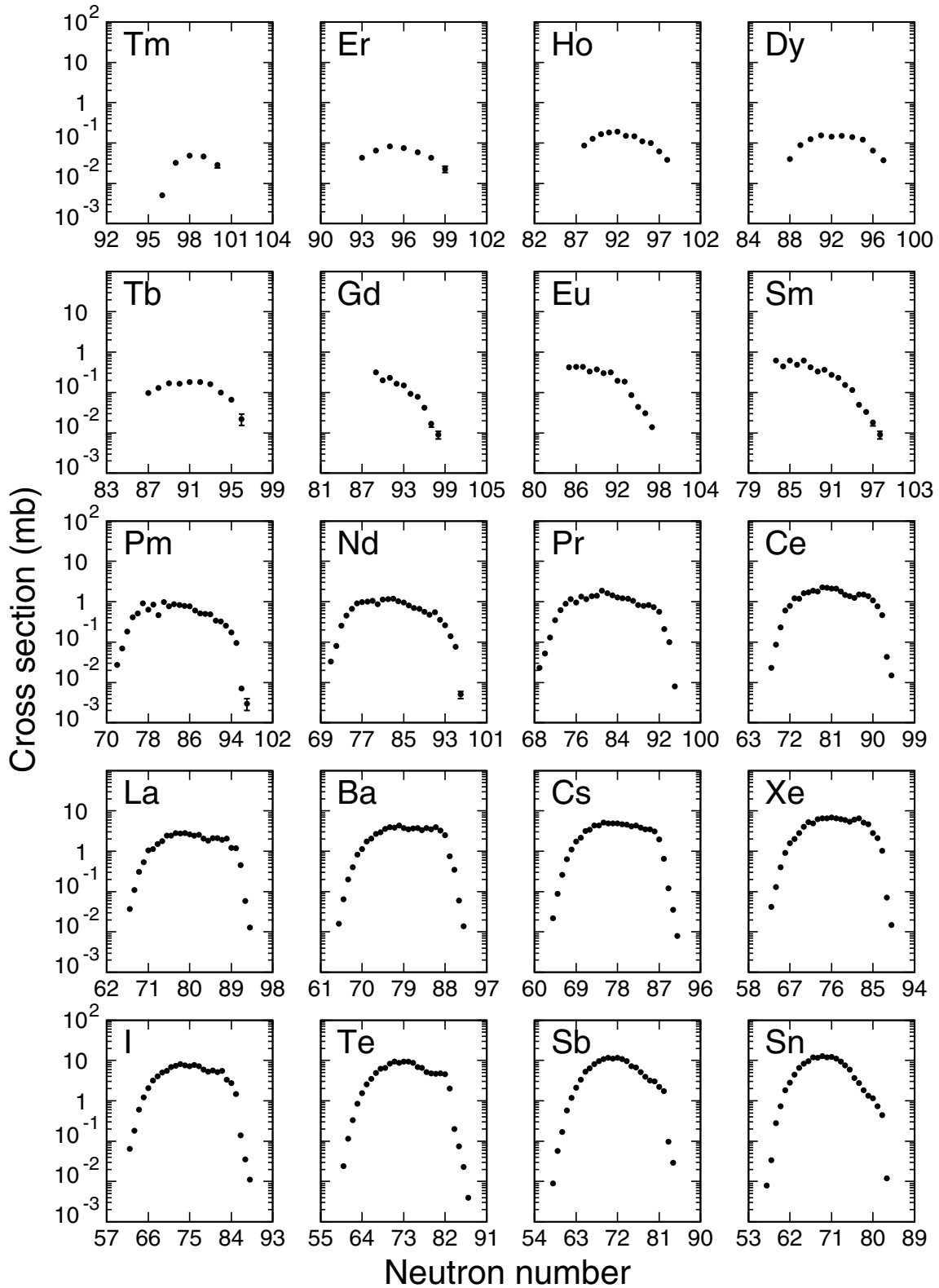


FIG. 14. Measured isotopic production cross sections of fission fragments, in the range $23 \leq Z \leq 69$, produced in the reaction $^{238}\text{U}(1\text{A GeV}) + d$. (Statistical errors are shown when larger than symbols.)

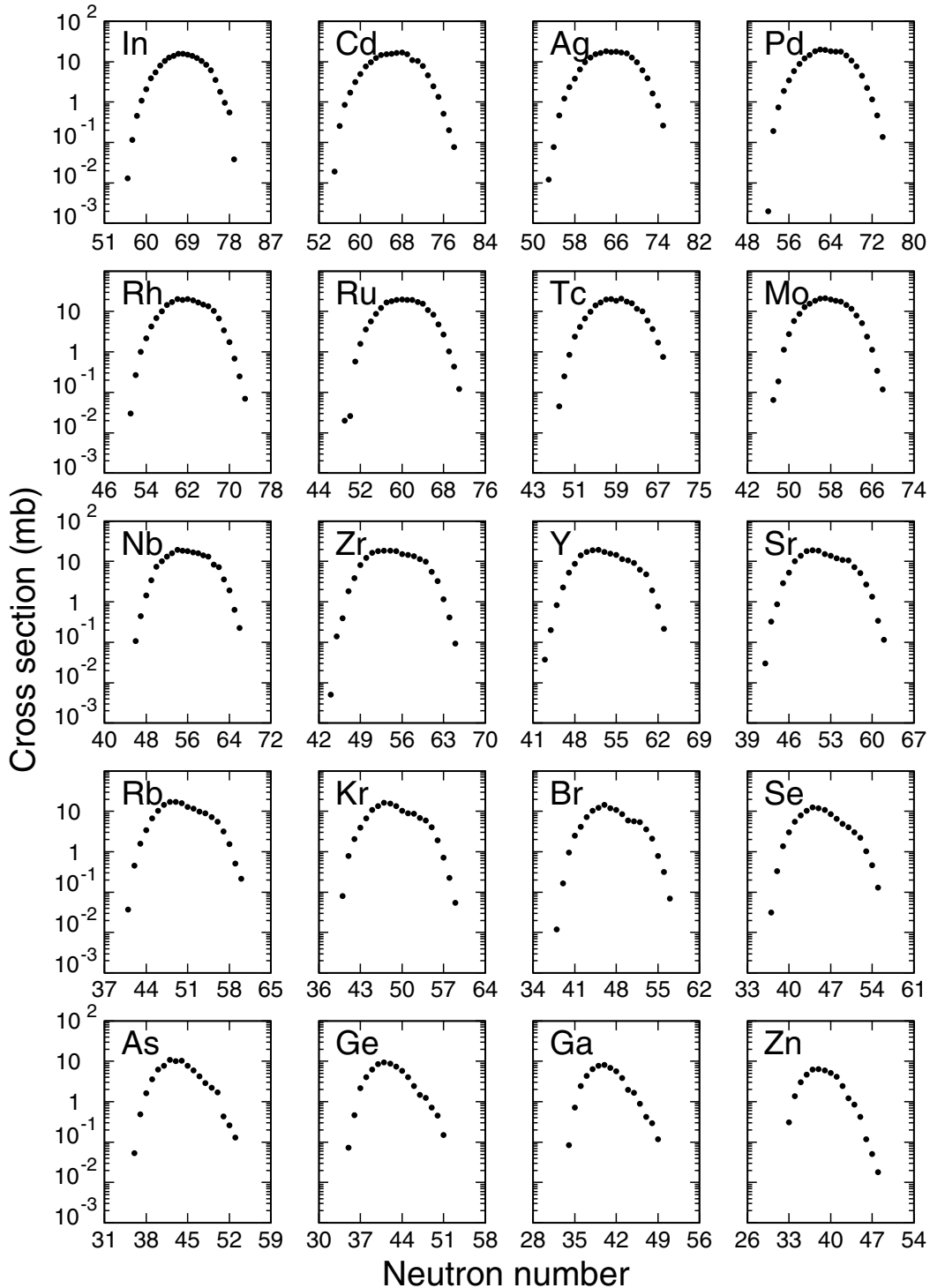


FIG. 15. Measured isotopic production cross sections of fission fragments, in the range $23 \leq Z \leq 69$, produced in the reaction $^{238}\text{U}(1\text{A GeV}) + d$. (Statistical errors are shown when larger than symbols.)

not a directly measured observable, but deduced by summing up the contributions from every fission fragment. The isotopic production cross sections of the fission fragments shown in Figs. 14–16 were obtained by applying different systematic corrections to the measured yields. Some of these corrections, like the angular transmission or the secondary reactions in

the target, vary considerably as a function of the atomic and mass numbers of the final nuclei, reaching very large values in some cases. Any uncertainty in the determination of these corrections affected the values of the isotopic cross sections, and consequently the value of the total cross section. The high level of agreement between the total fission cross section

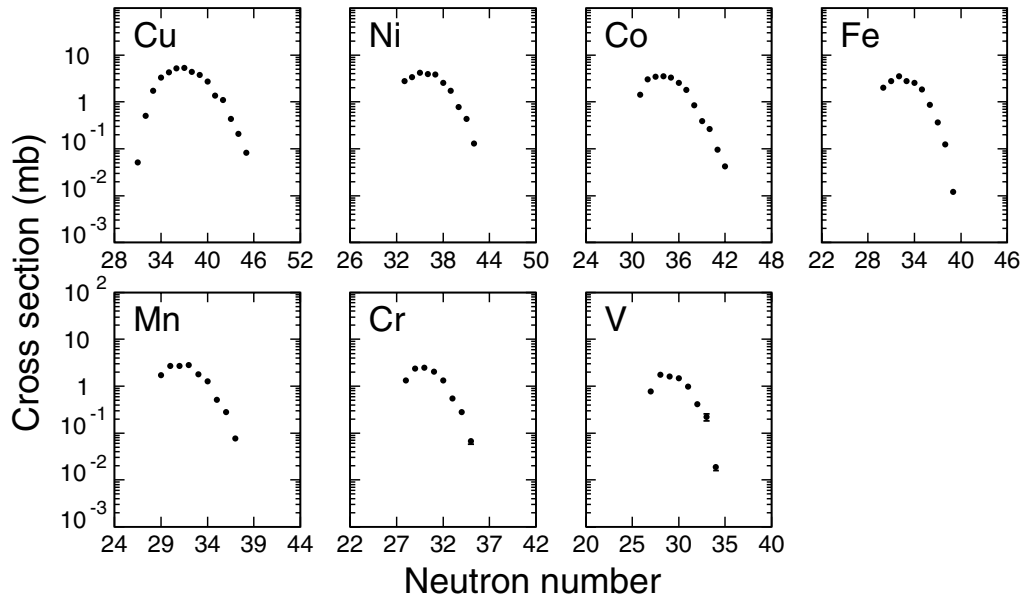


FIG. 16. Measured isotopic production cross sections of fission fragments, in the range $23 \leq Z \leq 69$, produced in the reaction $^{238}\text{U}(1\text{A GeV}) + d$. (Statistical errors are shown when larger than symbols.)

obtained in the present work and that deduced by extrapolation of a directly measured value [53] validates the methods used to determine these corrections. The 15% difference between the measured total reaction cross section and that calculated with Karol's model is within the uncertainty of our method.

V. CONCLUSION

In the present work, the spallation-fission fragments produced in the reaction $^{238}\text{U}(1\text{A GeV})$ on deuterium were experimentally investigated. The results obtained from the analysis include the evaluation of the velocities and isotopic production cross sections of 939 fission nuclei, which, together with the 602 evaporation fragments measured recently [12], constitutes one of the most extensive inventories of spallation-reaction productions ever measured before. The elements included in both experiments spread out over an extend region in the chart of the nuclides, ranging from vanadium ($Z = 23$) to thulium ($Z = 69$) for the fission case and from cerium ($Z = 58$) to neptunium ($N = 93$) for evaporation.

The precisions required for the present measurements were attainable only with the heavy-ion experimental facility at GSI, Darmstadt (Germany). The uranium beam, accelerated in the synchrotron accelerator SIS up to 1A GeV, was focused onto a cryogenic deuterium target placed at the entrance of the FRS, so that the forward-emitted fission fragments were transmitted through the separator. The optimum performance of the FRS, with a momentum resolving power of 1500, allowed the challenging separation of the reaction products, as well as their unambiguous identification according to the atomic and mass numbers.

The velocity distributions of the fission fragments were measured with relative resolutions of the order of 10^{-4} . Fits to these velocity distributions allowed for the separation of the kinematics from evaporation and fission components. The

results from the fits were introduced in an algorithm to extract the velocities of the fission fragment. The precisions attained with this technique ranged typically from 1 to 5%, reaching maximum values of 20% in cases of very poor statistics or high contamination from evaporation reactions. Within a given element, the isotopic dependence of the fission velocities revealed a contribution from many different fissioning systems to the total productions. Moreover, the relatively low velocities of some neutron-deficient isotopes were found to be a sign of the contamination from multiple reactions induced by primary fission fragments.

The isotopic production cross sections of the fission fragments were measured above the lower limit of $2 \mu\text{b}$, with statistical uncertainties ranging from 1% to 5% for the majority of the measured fragments. The systematic error induced by the different corrections applied to the measured isotopic productions covers a wide range that extends from 10% to 20%, for most of the nuclei, to maximum values of 50% for very few cases. The main source of systematic error were the corrections that accounted for the multiple reactions in the production target and for the contamination from evaporation reactions. The maximum value of the cross sections—around 30 mb—were found for intermediate-mass fragments around palladium ($Z = 46$). The isotopic chains of most of the fission fragments are well described by a Gaussian function with mean neutron numbers slightly shifted toward the neutron-rich side of the valley of stability. For some elements above $Z = 50$, a second maximum shows up in the neutron-rich isotopes, revealing a sizable population of the asymmetric fission channels by low-energy fission. When summing up the measured isotopic cross sections, a total value of $(2.00 \pm 0.42 \text{ b})$ was found, which is in good agreement with results obtained from Glauber-type models and extrapolations from experimental values. The addition of this cross section to the value of $(0.91 \pm 0.11 \text{ b})$ for the evaporation

component [12] yields a total value of $(2.91 \pm 0.43 \text{ b})$, which is in good agreement with Glauber-type calculations [40].

The richness of the present results demands a detailed discussion of the many different physical aspects underlying the investigated reaction.

ACKNOWLEDGMENTS

The authors thank K.-H. Behr, A. Brüne, and K. Burkard for their technical support during the experiment, as well as the

group of P. Chesny, who built the liquid-hydrogen/deuterium target. This work was partially supported by the Spanish Ministry of Education and Science and Xunta de Galicia under contracts FPA2002-04181-C04-01 and PGIDT01PXI20603PM, respectively, and the European Community under contracts “Access to Research Infrastructure Action of the Improving Human Potential” (PRICT-1999-00001), “HINDAS” (FIKW-CT-2000-00031), and “Research Infrastructure Action—Structuring the European Research Area” (EURISOL DS Project contract 515768 RIDS). The EC is not liable for any use that may be made of the information contained herein.

APPENDIX: VELOCITY AND ISOTOPIC PRODUCTION CROSS SECTIONS OF FISSION FRAGMENTS

TABLE I. Velocities of fission fragments (in cm/ns) measured in the frame of the fissioning system for the reaction $^{238}\text{U}(1A \text{ GeV}) + d$, with their total error.

Nucleus	v_{fiss} (cm/ns)	ε_{tot} (cm/ns)	Nucleus	v_{fiss} (cm/ns)	ε_{tot} (cm/ns)	Nucleus	v_{fiss} (cm/ns)	ε_{tot} (cm/ns)	Nucleus	v_{fiss} (cm/ns)	ε_{tot} (cm/ns)
^{49}V	1.590	0.070	^{65}Co	1.620	0.051	^{67}Ga	1.440	0.032	^{79}Se	1.470	0.010
^{50}V	1.690	0.020	^{66}Co	1.620	0.051	^{68}Ga	1.470	0.010	^{80}Se	1.470	0.010
^{51}V	1.720	0.022	^{67}Co	1.620	0.051	^{69}Ga	1.510	0.010	^{81}Se	1.460	0.014
^{52}V	1.700	0.010	^{68}Co	1.620	0.081	^{70}Ga	1.530	0.014	^{82}Se	1.460	0.014
^{53}V	1.750	0.030	^{69}Co	1.620	0.081	^{71}Ga	1.520	0.014	^{83}Se	1.450	0.032
^{54}V	1.760	0.010	^{57}Ni	0.870	0.150	^{72}Ga	1.520	0.014	^{84}Se	1.450	0.041
^{55}V	1.710	0.040	^{58}Ni	1.030	0.120	^{73}Ga	1.540	0.014	^{85}Se	1.450	0.014
^{56}V	1.710	0.100	^{59}Ni	1.250	0.071	^{74}Ga	1.540	0.014	^{86}Se	1.480	0.014
^{57}V	1.710	0.100	^{60}Ni	1.400	0.020	^{75}Ga	1.540	0.030	^{87}Se	1.490	0.010
^{49}Cr	0.840	0.150	^{61}Ni	1.470	0.032	^{76}Ga	1.540	0.030	^{88}Se	1.490	0.030
^{50}Cr	1.140	0.120	^{62}Ni	1.530	0.010	^{77}Ga	1.540	0.032	^{89}Se	1.480	0.041
^{51}Cr	1.450	0.090	^{63}Ni	1.570	0.014	^{78}Ga	1.540	0.032	^{73}Br	1.110	0.091
^{52}Cr	1.630	0.050	^{64}Ni	1.590	0.010	^{79}Ga	1.540	0.051	^{74}Br	1.200	0.071
^{53}Cr	1.700	0.010	^{65}Ni	1.610	0.010	^{80}Ga	1.540	0.061	^{75}Br	1.290	0.060
^{54}Cr	1.690	0.010	^{66}Ni	1.630	0.010	^{67}Ge	1.090	0.120	^{76}Br	1.310	0.030
^{55}Cr	1.720	0.010	^{67}Ni	1.600	0.014	^{68}Ge	1.300	0.080	^{77}Br	1.360	0.014
^{56}Cr	1.690	0.010	^{68}Ni	1.600	0.071	^{69}Ge	1.400	0.061	^{78}Br	1.400	0.014
^{57}Cr	1.690	0.050	^{69}Ni	1.620	0.060	^{70}Ge	1.440	0.040	^{79}Br	1.410	0.014
^{58}Cr	1.690	0.060	^{70}Ni	1.640	0.022	^{71}Ge	1.490	0.010	^{80}Br	1.420	0.014
^{59}Cr	1.690	0.080	^{71}Ni	1.620	0.070	^{72}Ge	1.520	0.010	^{81}Br	1.410	0.022
^{51}Mn	0.880	0.160	^{72}Ni	1.620	0.100	^{73}Ge	1.490	0.014	^{82}Br	1.410	0.020
^{52}Mn	1.110	0.130	^{59}Cu	1.010	0.160	^{74}Ge	1.520	0.014	^{83}Br	1.450	0.010
^{53}Mn	1.520	0.120	^{60}Cu	1.150	0.120	^{75}Ge	1.520	0.014	^{84}Br	1.450	0.010
^{54}Mn	1.660	0.050	^{61}Cu	1.340	0.100	^{76}Ge	1.510	0.010	^{85}Br	1.450	0.050
^{55}Mn	1.670	0.010	^{62}Cu	1.450	0.061	^{77}Ge	1.540	0.010	^{86}Br	1.450	0.030
^{56}Mn	1.710	0.022	^{63}Cu	1.530	0.022	^{78}Ge	1.520	0.050	^{87}Br	1.470	0.010
^{57}Mn	1.690	0.014	^{64}Cu	1.550	0.014	^{79}Ge	1.520	0.050	^{88}Br	1.470	0.010
^{58}Mn	1.650	0.010	^{65}Cu	1.570	0.014	^{80}Ge	1.500	0.014	^{89}Br	1.470	0.010
^{59}Mn	1.690	0.010	^{66}Cu	1.550	0.014	^{81}Ge	1.510	0.014	^{90}Br	1.450	0.010
^{60}Mn	1.650	0.014	^{67}Cu	1.560	0.010	^{82}Ge	1.520	0.014	^{91}Br	1.450	0.030
^{61}Mn	1.650	0.022	^{68}Cu	1.580	0.014	^{83}Ge	1.520	0.041	^{92}Br	1.450	0.040
^{62}Mn	1.650	0.051	^{69}Cu	1.600	0.010	^{69}As	1.100	0.090	^{76}Kr	1.150	0.071
^{63}Mn	1.640	0.051	^{70}Cu	1.550	0.030	^{70}As	1.270	0.050	^{77}Kr	1.230	0.061
^{53}Fe	0.860	0.150	^{71}Cu	1.550	0.040	^{71}As	1.340	0.030	^{78}Kr	1.280	0.032
^{54}Fe	1.160	0.100	^{72}Cu	1.610	0.060	^{72}As	1.410	0.022	^{79}Kr	1.330	0.010
^{55}Fe	1.450	0.070	^{73}Cu	1.610	0.070	^{73}As	1.420	0.014	^{80}Kr	1.340	0.010
^{56}Fe	1.570	0.022	^{74}Cu	1.610	0.071	^{74}As	1.430	0.014	^{81}Kr	1.370	0.010
^{57}Fe	1.650	0.070	^{62}Zn	1.010	0.120	^{75}As	1.480	0.030	^{82}Kr	1.370	0.014
^{58}Fe	1.620	0.010	^{63}Zn	1.210	0.091	^{76}As	1.460	0.022	^{83}Kr	1.400	0.014
^{59}Fe	1.610	0.010	^{64}Zn	1.370	0.022	^{77}As	1.480	0.010	^{84}Kr	1.400	0.014

TABLE I. (*Continued.*)

Nucleus	v_{fiss} (cm/ns)	ϵ_{tot} (cm/ns)	Nucleus	v_{fiss} (cm/ns)	ϵ_{tot} (cm/ns)	Nucleus	v_{fiss} (cm/ns)	ϵ_{tot} (cm/ns)	Nucleus	v_{fiss} (cm/ns)	ϵ_{tot} (cm/ns)
^{60}Fe	1.610	0.020	^{65}Zn	1.430	0.014	^{78}As	1.480	0.010	^{85}Kr	1.410	0.014
^{61}Fe	1.620	0.050	^{66}Zn	1.520	0.010	^{79}As	1.490	0.010	^{86}Kr	1.400	0.014
^{62}Fe	1.600	0.051	^{67}Zn	1.520	0.014	^{80}As	1.490	0.040	^{87}Kr	1.400	0.014
^{63}Fe	1.600	0.051	^{68}Zn	1.540	0.010	^{81}As	1.490	0.030	^{88}Kr	1.420	0.040
^{64}Fe	1.600	0.061	^{69}Zn	1.550	0.010	^{82}As	1.490	0.010	^{89}Kr	1.420	0.010
^{65}Fe	1.600	0.041	^{70}Zn	1.530	0.010	^{83}As	1.470	0.010	^{90}Kr	1.430	0.014
^{66}Fe	1.600	0.041	^{71}Zn	1.560	0.010	^{84}As	1.470	0.010	^{91}Kr	1.420	0.010
^{55}Co	0.820	0.150	^{72}Zn	1.570	0.020	^{85}As	1.490	0.014	^{92}Kr	1.400	0.010
^{56}Co	1.030	0.120	^{73}Zn	1.570	0.040	^{86}As	1.500	0.050	^{93}Kr	1.430	0.014
^{57}Co	1.340	0.081	^{74}Zn	1.570	0.040	^{71}Se	1.060	0.091	^{94}Kr	1.410	0.014
^{58}Co	1.540	0.010	^{75}Zn	1.570	0.014	^{72}Se	1.220	0.071	^{95}Kr	1.410	0.041
^{59}Co	1.600	0.030	^{76}Zn	1.580	0.040	^{73}Se	1.280	0.010	^{78}Rb	1.070	0.100
^{60}Co	1.630	0.030	^{77}Zn	1.580	0.050	^{74}Se	1.330	0.010	^{79}Rb	1.180	0.070
^{61}Co	1.630	0.030	^{78}Zn	1.580	0.050	^{75}Se	1.390	0.014	^{80}Rb	1.280	0.040
^{62}Co	1.620	0.050	^{64}Ga	0.960	0.110	^{76}Se	1.430	0.010	^{81}Rb	1.310	0.022
^{63}Co	1.620	0.051	^{65}Ga	1.210	0.081	^{77}Se	1.440	0.010	^{82}Rb	1.330	0.014
^{64}Co	1.620	0.051	^{66}Ga	1.320	0.071	^{78}Se	1.450	0.010	^{83}Rb	1.340	0.010

TABLE II. Velocities of fission fragments (in cm/ns) measured in the frame of the fissioning system for the reaction $^{238}\text{U}(1\text{A GeV}) + d$, with their total error.

Nucleus	v_{fiss} (cm/ns)	ϵ_{tot} (cm/ns)	Nucleus	v_{fiss} (cm/ns)	ϵ_{tot} (cm/ns)	Nucleus	v_{fiss} (cm/ns)	ϵ_{tot} (cm/ns)	Nucleus	v_{fiss} (cm/ns)	ϵ_{tot} (cm/ns)
^{84}Rb	1.370	0.010	^{85}Zr	1.090	0.071	^{104}Mo	1.270	0.032	^{102}Rh	1.110	0.014
^{85}Rb	1.380	0.022	^{86}Zr	1.110	0.051	^{105}Mo	1.270	0.020	^{103}Rh	1.150	0.010
^{86}Rb	1.370	0.010	^{87}Zr	1.170	0.030	^{106}Mo	1.270	0.015	^{104}Rh	1.150	0.014
^{87}Rb	1.380	0.010	^{88}Zr	1.190	0.030	^{107}Mo	1.280	0.015	^{105}Rh	1.170	0.020
^{88}Rb	1.370	0.014	^{89}Zr	1.210	0.010	^{108}Mo	1.280	0.015	^{106}Rh	1.170	0.014
^{89}Rb	1.400	0.032	^{90}Zr	1.230	0.014	^{109}Mo	1.270	0.020	^{107}Rh	1.170	0.010
^{90}Rb	1.420	0.030	^{91}Zr	1.260	0.014	^{110}Mo	1.280	0.020	^{108}Rh	1.180	0.010
^{91}Rb	1.400	0.041	^{92}Zr	1.260	0.014	^{91}Tc	0.910	0.100	^{109}Rh	1.200	0.014
^{92}Rb	1.400	0.022	^{93}Zr	1.260	0.010	^{92}Tc	1.020	0.061	^{110}Rh	1.200	0.014
^{93}Rb	1.420	0.014	^{94}Zr	1.280	0.014	^{93}Tc	1.090	0.032	^{111}Rh	1.200	0.030
^{94}Rb	1.420	0.010	^{95}Zr	1.290	0.015	^{94}Tc	1.110	0.014	^{112}Rh	1.200	0.030
^{95}Rb	1.400	0.020	^{96}Zr	1.290	0.014	^{95}Tc	1.130	0.014	^{113}Rh	1.190	0.030
^{96}Rb	1.390	0.020	^{97}Zr	1.310	0.020	^{96}Tc	1.140	0.014	^{114}Rh	1.190	0.020
^{97}Rb	1.370	0.020	^{98}Zr	1.300	0.035	^{97}Tc	1.160	0.020	^{115}Rh	1.180	0.014
^{80}Sr	1.100	0.071	^{99}Zr	1.290	0.041	^{98}Tc	1.190	0.020	^{116}Rh	1.180	0.014
^{81}Sr	1.160	0.061	^{100}Zr	1.310	0.032	^{99}Tc	1.190	0.030	^{117}Rh	1.190	0.032
^{82}Sr	1.190	0.061	^{101}Zr	1.320	0.030	^{100}Tc	1.220	0.030	^{118}Rh	1.190	0.041
^{83}Sr	1.240	0.030	^{102}Zr	1.340	0.014	^{101}Tc	1.220	0.010	^{99}Pd	0.970	0.050
^{84}Sr	1.280	0.010	^{103}Zr	1.340	0.014	^{102}Tc	1.220	0.014	^{100}Pd	1.000	0.030
^{85}Sr	1.310	0.014	^{104}Zr	1.340	0.014	^{103}Tc	1.230	0.010	^{101}Pd	1.020	0.032
^{86}Sr	1.320	0.010	^{105}Zr	1.350	0.032	^{104}Tc	1.240	0.014	^{102}Pd	1.070	0.032
^{87}Sr	1.320	0.010	^{87}Nb	1.060	0.080	^{105}Tc	1.220	0.020	^{103}Pd	1.070	0.022
^{88}Sr	1.350	0.010	^{88}Nb	1.100	0.051	^{106}Tc	1.210	0.020	^{104}Pd	1.090	0.022
^{89}Sr	1.360	0.014	^{89}Nb	1.140	0.014	^{107}Tc	1.220	0.020	^{105}Pd	1.090	0.014
^{90}Sr	1.360	0.014	^{90}Nb	1.160	0.010	^{108}Tc	1.220	0.025	^{106}Pd	1.110	0.014
^{91}Sr	1.380	0.010	^{91}Nb	1.220	0.032	^{109}Tc	1.220	0.025	^{107}Pd	1.100	0.010
^{92}Sr	1.380	0.010	^{92}Nb	1.220	0.014	^{110}Tc	1.210	0.020	^{108}Pd	1.140	0.014
^{93}Sr	1.380	0.040	^{93}Nb	1.240	0.010	^{111}Tc	1.220	0.025	^{109}Pd	1.150	0.014
^{94}Sr	1.380	0.030	^{94}Nb	1.230	0.014	^{93}Ru	0.990	0.100	^{110}Pd	1.140	0.022
^{95}Sr	1.390	0.020	^{95}Nb	1.260	0.010	^{94}Ru	1.000	0.061	^{111}Pd	1.150	0.020

TABLE II. (Continued.)

Nucleus	v_{fiss} (cm/ns)	ε_{tot} (cm/ns)	Nucleus	v_{fiss} (cm/ns)	ε_{tot} (cm/ns)	Nucleus	v_{fiss} (cm/ns)	ε_{tot} (cm/ns)	Nucleus	v_{fiss} (cm/ns)	ε_{tot} (cm/ns)
⁹⁶ Sr	1.390	0.010	⁹⁶ Nb	1.270	0.014	⁹⁵ Ru	1.030	0.032	¹¹² Pd	1.140	0.010
⁹⁷ Sr	1.390	0.014	⁹⁷ Nb	1.270	0.010	⁹⁶ Ru	1.080	0.041	¹¹³ Pd	1.140	0.020
⁹⁸ Sr	1.370	0.015	⁹⁸ Nb	1.290	0.010	⁹⁷ Ru	1.130	0.032	¹¹⁴ Pd	1.140	0.022
⁹⁹ Sr	1.350	0.017	⁹⁹ Nb	1.290	0.014	⁹⁸ Ru	1.130	0.022	¹¹⁵ Pd	1.130	0.032
¹⁰⁰ Sr	1.350	0.020	¹⁰⁰ Nb	1.290	0.014	⁹⁹ Ru	1.140	0.014	¹¹⁶ Pd	1.140	0.022
⁸² Y	1.010	0.150	¹⁰¹ Nb	1.290	0.032	¹⁰⁰ Ru	1.160	0.014	¹¹⁷ Pd	1.140	0.022
⁸³ Y	1.140	0.091	¹⁰² Nb	1.270	0.032	¹⁰¹ Ru	1.180	0.014	¹¹⁸ Pd	1.170	0.022
⁸⁴ Y	1.200	0.050	¹⁰³ Nb	1.290	0.014	¹⁰² Ru	1.170	0.010	¹¹⁹ Pd	1.160	0.014
⁸⁵ Y	1.210	0.030	¹⁰⁴ Nb	1.290	0.014	¹⁰³ Ru	1.190	0.014	¹²⁰ Pd	1.160	0.032
⁸⁶ Y	1.230	0.020	¹⁰⁵ Nb	1.300	0.015	¹⁰⁴ Ru	1.190	0.014	¹⁰¹ Ag	0.910	0.032
⁸⁷ Y	1.260	0.014	¹⁰⁶ Nb	1.300	0.020	¹⁰⁵ Ru	1.190	0.022	¹⁰² Ag	0.930	0.022
⁸⁸ Y	1.270	0.014	¹⁰⁷ Nb	1.290	0.030	¹⁰⁶ Ru	1.210	0.014	¹⁰³ Ag	0.970	0.014
⁸⁹ Y	1.310	0.010	⁸⁹ Mo	1.010	0.091	¹⁰⁷ Ru	1.220	0.014	¹⁰⁴ Ag	0.970	0.032
⁹⁰ Y	1.310	0.010	⁹⁰ Mo	1.050	0.051	¹⁰⁸ Ru	1.220	0.022	¹⁰⁵ Ag	1.020	0.030
⁹¹ Y	1.340	0.010	⁹¹ Mo	1.110	0.041	¹⁰⁹ Ru	1.220	0.032	¹⁰⁶ Ag	1.040	0.010
⁹² Y	1.340	0.014	⁹² Mo	1.160	0.010	¹¹⁰ Ru	1.210	0.030	¹⁰⁷ Ag	1.080	0.022
⁹³ Y	1.330	0.014	⁹³ Mo	1.190	0.010	¹¹¹ Ru	1.210	0.014	¹⁰⁸ Ag	1.090	0.014
⁹⁴ Y	1.360	0.041	⁹⁴ Mo	1.190	0.014	¹¹² Ru	1.210	0.022	¹⁰⁹ Ag	1.090	0.014
⁹⁵ Y	1.320	0.032	⁹⁵ Mo	1.220	0.014	¹¹³ Ru	1.220	0.014	¹¹⁰ Ag	1.100	0.014
⁹⁶ Y	1.340	0.041	⁹⁶ Mo	1.220	0.014	¹¹⁴ Ru	1.220	0.014	¹¹¹ Ag	1.130	0.010
⁹⁷ Y	1.350	0.040	⁹⁷ Mo	1.230	0.014	¹¹⁵ Ru	1.220	0.014	¹¹² Ag	1.130	0.014
⁹⁸ Y	1.340	0.022	⁹⁸ Mo	1.250	0.010	⁹⁶ Rh	0.920	0.081	¹¹³ Ag	1.120	0.014
⁹⁹ Y	1.360	0.010	⁹⁹ Mo	1.260	0.010	⁹⁷ Rh	0.970	0.051	¹¹⁴ Ag	1.130	0.014
¹⁰⁰ Y	1.340	0.015	¹⁰⁰ Mo	1.280	0.014	⁹⁸ Rh	0.980	0.051	¹¹⁵ Ag	1.150	0.010
¹⁰¹ Y	1.340	0.015	¹⁰¹ Mo	1.260	0.010	⁹⁹ Rh	1.030	0.030	¹¹⁶ Ag	1.150	0.020
¹⁰² Y	1.330	0.015	¹⁰² Mo	1.270	0.010	¹⁰⁰ Rh	1.080	0.010	¹¹⁷ Ag	1.130	0.032
⁸⁴ Zr	0.940	0.100	¹⁰³ Mo	1.270	0.022	¹⁰¹ Rh	1.100	0.014	¹¹⁸ Ag	1.130	0.032

TABLE III. Velocities of fission fragments (in cm/ns) measured in the frame of the fissioning system for the reaction ²³⁸U(1A GeV) + d, with their total error.

Nucleus	v_{fiss} (cm/ns)	ε_{tot} (cm/ns)	Nucleus	v_{fiss} (cm/ns)	ε_{tot} (cm/ns)	Nucleus	v_{fiss} (cm/ns)	ε_{tot} (cm/ns)	Nucleus	v_{fiss} (cm/ns)	ε_{tot} (cm/ns)
¹¹⁹ Ag	1.130	0.022	¹¹³ Sn	0.960	0.022	¹²¹ Te	0.970	0.036	¹²⁹ Xe	0.960	0.014
¹²⁰ Ag	1.140	0.032	¹¹⁴ Sn	1.010	0.014	¹²² Te	0.990	0.010	¹³⁰ Xe	0.990	0.020
¹²¹ Ag	1.140	0.014	¹¹⁵ Sn	1.020	0.010	¹²³ Te	0.990	0.014	¹³¹ Xe	0.970	0.022
¹²² Ag	1.140	0.032	¹¹⁶ Sn	1.020	0.014	¹²⁴ Te	1.000	0.010	¹³² Xe	0.970	0.014
¹⁰³ Cd	0.920	0.051	¹¹⁷ Sn	1.020	0.014	¹²⁵ Te	1.000	0.014	¹³³ Xe	0.980	0.014
¹⁰⁴ Cd	0.960	0.040	¹¹⁸ Sn	1.020	0.010	¹²⁶ Te	1.010	0.014	¹³⁴ Xe	0.970	0.022
¹⁰⁵ Cd	0.970	0.032	¹¹⁹ Sn	1.030	0.014	¹²⁷ Te	1.020	0.010	¹³⁵ Xe	0.980	0.014
¹⁰⁶ Cd	1.000	0.020	¹²⁰ Sn	1.040	0.014	¹²⁸ Te	1.020	0.022	¹³⁶ Xe	0.990	0.040
¹⁰⁷ Cd	1.000	0.010	¹²¹ Sn	1.030	0.014	¹²⁹ Te	1.010	0.022	¹³⁷ Xe	0.980	0.014
¹⁰⁸ Cd	1.020	0.032	¹²² Sn	1.040	0.014	¹³⁰ Te	1.000	0.041	¹³⁸ Xe	0.980	0.022
¹⁰⁹ Cd	1.030	0.010	¹²³ Sn	1.030	0.014	¹³¹ Te	1.010	0.041	¹³⁹ Xe	0.950	0.020
¹¹⁰ Cd	1.030	0.014	¹²⁴ Sn	1.020	0.032	¹³² Te	1.010	0.032	¹⁴⁰ Xe	0.940	0.032
¹¹¹ Cd	1.030	0.014	¹²⁵ Sn	1.040	0.032	¹³³ Te	1.020	0.015	¹⁴¹ Xe	0.970	0.022
¹¹² Cd	1.060	0.014	¹²⁶ Sn	1.040	0.032	¹³⁴ Te	1.030	0.022	¹⁴² Xe	0.950	0.022
¹¹³ Cd	1.060	0.014	¹²⁷ Sn	1.050	0.012	¹³⁵ Te	1.040	0.022	¹⁴³ Xe	0.940	0.041
¹¹⁴ Cd	1.080	0.010	¹²⁸ Sn	1.060	0.012	¹³⁶ Te	1.050	0.015	¹¹⁹ Cs	0.480	0.190
¹¹⁵ Cd	1.110	0.010	¹²⁹ Sn	1.070	0.014	¹³⁷ Te	1.050	0.015	¹²⁰ Cs	0.650	0.081
¹¹⁶ Cd	1.110	0.014	¹³⁰ Sn	1.070	0.014	¹³⁸ Te	1.040	0.020	¹²¹ Cs	0.700	0.041
¹¹⁷ Cd	1.130	0.010	¹³¹ Sn	1.070	0.014	¹³⁹ Te	1.040	0.032	¹²² Cs	0.740	0.014
¹¹⁸ Cd	1.120	0.030	¹³² Sn	1.070	0.014	¹¹⁶ I	0.630	0.100	¹²³ Cs	0.790	0.022
¹¹⁹ Cd	1.110	0.032	¹³³ Sn	1.060	0.014	¹¹⁷ I	0.770	0.071	¹²⁴ Cs	0.830	0.022

TABLE III. (*Continued.*)

Nucleus	v_{fiss} (cm/ns)	ε_{tot} (cm/ns)	Nucleus	v_{fiss} (cm/ns)	ε_{tot} (cm/ns)	Nucleus	v_{fiss} (cm/ns)	ε_{tot} (cm/ns)	Nucleus	v_{fiss} (cm/ns)	ε_{tot} (cm/ns)
¹²⁰ Cd	1.120	0.020	¹⁰⁹ Sb	0.660	0.081	¹¹⁸ I	0.830	0.032	¹²⁵ Cs	0.850	0.022
¹²¹ Cd	1.110	0.032	¹¹⁰ Sb	0.750	0.032	¹¹⁹ I	0.880	0.041	¹²⁶ Cs	0.890	0.022
¹²² Cd	1.110	0.020	¹¹¹ Sb	0.780	0.032	¹²⁰ I	0.910	0.032	¹²⁷ Cs	0.910	0.022
¹²³ Cd	1.120	0.022	¹¹² Sb	0.850	0.022	¹²¹ I	0.910	0.014	¹²⁸ Cs	0.910	0.014
¹²⁴ Cd	1.110	0.014	¹¹³ Sb	0.880	0.014	¹²² I	0.940	0.022	¹²⁹ Cs	0.900	0.014
¹²⁵ Cd	1.100	0.022	¹¹⁴ Sb	0.900	0.014	¹²³ I	0.950	0.014	¹³⁰ Cs	0.910	0.014
¹²⁶ Cd	1.100	0.032	¹¹⁵ Sb	0.930	0.010	¹²⁴ I	0.960	0.014	¹³¹ Cs	0.920	0.014
¹⁰⁶ In	0.800	0.081	¹¹⁶ Sb	0.970	0.014	¹²⁵ I	0.970	0.010	¹³² Cs	0.920	0.014
¹⁰⁷ In	0.880	0.051	¹¹⁷ Sb	0.970	0.014	¹²⁶ I	0.970	0.010	¹³³ Cs	0.920	0.014
¹⁰⁸ In	0.890	0.041	¹¹⁸ Sb	1.000	0.014	¹²⁷ I	0.960	0.010	¹³⁴ Cs	0.920	0.014
¹⁰⁹ In	0.930	0.020	¹¹⁹ Sb	1.020	0.014	¹²⁸ I	0.970	0.014	¹³⁵ Cs	0.920	0.014
¹¹⁰ In	0.980	0.014	¹²⁰ Sb	1.020	0.014	¹²⁹ I	0.990	0.014	¹³⁶ Cs	0.900	0.032
¹¹¹ In	0.980	0.014	¹²¹ Sb	1.040	0.022	¹³⁰ I	0.990	0.014	¹³⁷ Cs	0.900	0.041
¹¹² In	1.030	0.010	¹²² Sb	1.020	0.032	¹³¹ I	0.990	0.014	¹³⁸ Cs	0.910	0.014
¹¹³ In	1.050	0.014	¹²³ Sb	1.050	0.010	¹³² I	0.980	0.014	¹³⁹ Cs	0.900	0.032
¹¹⁴ In	1.050	0.014	¹²⁴ Sb	1.050	0.014	¹³³ I	1.000	0.032	¹⁴⁰ Cs	0.890	0.022
¹¹⁵ In	1.070	0.014	¹²⁵ Sb	1.040	0.014	¹³⁴ I	0.980	0.032	¹⁴¹ Cs	0.910	0.014
¹¹⁶ In	1.100	0.010	¹²⁶ Sb	1.040	0.014	¹³⁵ I	1.010	0.022	¹⁴² Cs	0.910	0.014
¹¹⁷ In	1.100	0.010	¹²⁷ Sb	1.040	0.014	¹³⁶ I	0.990	0.014	¹⁴³ Cs	0.910	0.014
¹¹⁸ In	1.090	0.014	¹²⁸ Sb	1.030	0.032	¹³⁷ I	1.020	0.020	¹⁴⁴ Cs	0.920	0.022
¹¹⁹ In	1.100	0.014	¹²⁹ Sb	1.050	0.014	¹³⁸ I	0.990	0.010	¹⁴⁵ Cs	0.910	0.022
¹²⁰ In	1.100	0.010	¹³⁰ Sb	1.060	0.010	¹³⁹ I	0.990	0.014	¹⁴⁶ Cs	0.910	0.032
¹²¹ In	1.100	0.020	¹³¹ Sb	1.060	0.010	¹⁴⁰ I	0.990	0.022	¹²¹ Ba	0.400	0.200
¹²² In	1.110	0.032	¹³² Sb	1.060	0.014	¹⁴¹ I	0.990	0.051	¹²² Ba	0.530	0.090
¹²³ In	1.110	0.032	¹³³ Sb	1.070	0.014	¹¹⁷ Xe	0.540	0.130	¹²³ Ba	0.650	0.041
¹²⁴ In	1.100	0.022	¹³⁴ Sb	1.060	0.014	¹¹⁸ Xe	0.690	0.071	¹²⁴ Ba	0.700	0.022
¹²⁵ In	1.090	0.022	¹³⁵ Sb	1.050	0.032	¹¹⁹ Xe	0.740	0.041	¹²⁵ Ba	0.730	0.022
¹²⁶ In	1.110	0.020	¹¹² Te	0.720	0.051	¹²⁰ Xe	0.780	0.014	¹²⁶ Ba	0.750	0.022
¹²⁷ In	1.090	0.014	¹¹³ Te	0.740	0.041	¹²¹ Xe	0.830	0.051	¹²⁷ Ba	0.790	0.014
¹²⁸ In	1.090	0.022	¹¹⁴ Te	0.800	0.022	¹²² Xe	0.860	0.014	¹²⁸ Ba	0.850	0.028
¹⁰⁷ Sn	0.700	0.061	¹¹⁵ Te	0.830	0.014	¹²³ Xe	0.870	0.022	¹²⁹ Ba	0.860	0.022
¹⁰⁸ Sn	0.780	0.032	¹¹⁶ Te	0.860	0.014	¹²⁴ Xe	0.900	0.014	¹³⁰ Ba	0.890	0.014
¹⁰⁹ Sn	0.820	0.014	¹¹⁷ Te	0.880	0.014	¹²⁵ Xe	0.930	0.014	¹³¹ Ba	0.880	0.022
¹¹⁰ Sn	0.860	0.014	¹¹⁸ Te	0.900	0.014	¹²⁶ Xe	0.930	0.014	¹³² Ba	0.920	0.014
¹¹¹ Sn	0.910	0.014	¹¹⁹ Te	0.920	0.024	¹²⁷ Xe	0.950	0.014	¹³³ Ba	0.920	0.014
¹¹² Sn	0.950	0.014	¹²⁰ Te	0.940	0.042	¹²⁸ Xe	0.960	0.014	¹³⁴ Ba	0.930	0.028

TABLE IV. Velocities of fission fragments (in cm/ns) measured in the frame of the fissioning system for the reaction ²³⁸U(1A GeV) + *d*, with their total error.

Nucleus	v_{fiss} (cm/ns)	ε_{tot} (cm/ns)	Nucleus	v_{fiss} (cm/ns)	ε_{tot} (cm/ns)	Nucleus	v_{fiss} (cm/ns)	ε_{tot} (cm/ns)	Nucleus	v_{fiss} (cm/ns)	ε_{tot} (cm/ns)
¹³⁵ Ba	0.910	0.020	¹³⁷ Ce	0.860	0.014	¹⁴⁰ Nd	0.740	0.014	¹⁴⁷ Sm	0.740	0.022
¹³⁶ Ba	0.900	0.014	¹³⁸ Ce	0.860	0.014	¹⁴¹ Nd	0.750	0.014	¹⁴⁸ Sm	0.760	0.014
¹³⁷ Ba	0.920	0.014	¹³⁹ Ce	0.850	0.014	¹⁴² Nd	0.780	0.014	¹⁴⁹ Sm	0.760	0.014
¹³⁸ Ba	0.910	0.014	¹⁴⁰ Ce	0.860	0.014	¹⁴² Nd	0.780	0.014	¹⁵⁰ Sm	0.760	0.014
¹³⁹ Ba	0.910	0.014	¹⁴¹ Ce	0.860	0.014	¹⁴³ Nd	0.760	0.014	¹⁵¹ Sm	0.760	0.014
¹⁴⁰ Ba	0.920	0.014	¹⁴² Ce	0.870	0.014	¹⁴⁴ Nd	0.790	0.014	¹⁵² Sm	0.760	0.014
¹⁴¹ Ba	0.910	0.014	¹⁴³ Ce	0.880	0.014	¹⁴⁵ Nd	0.800	0.010	¹⁵³ Sm	0.770	0.010
¹⁴² Ba	0.920	0.014	¹⁴⁴ Ce	0.860	0.014	¹⁴⁶ Nd	0.800	0.022	¹⁵⁴ Sm	0.780	0.014
¹⁴³ Ba	0.910	0.014	¹⁴⁵ Ce	0.860	0.022	¹⁴⁷ Nd	0.810	0.014	¹⁵⁵ Sm	0.780	0.014
¹⁴⁴ Ba	0.910	0.014	¹⁴⁶ Ce	0.860	0.022	¹⁴⁸ Nd	0.820	0.014	¹⁵⁶ Sm	0.770	0.022

TABLE IV. (Continued.)

Nucleus	v_{fiss} (cm/ns)	ε_{tot} (cm/ns)	Nucleus	v_{fiss} (cm/ns)	ε_{tot} (cm/ns)	Nucleus	v_{fiss} (cm/ns)	ε_{tot} (cm/ns)	Nucleus	v_{fiss} (cm/ns)	ε_{tot} (cm/ns)
¹⁴⁵ Ba	0.890	0.014	¹⁴⁷ Ce	0.860	0.014	¹⁴⁹ Nd	0.820	0.014	¹⁵⁷ Sm	0.770	0.032
¹⁴⁶ Ba	0.890	0.014	¹⁴⁸ Ce	0.860	0.014	¹⁵⁰ Nd	0.830	0.022	¹⁵⁸ Sm	0.760	0.061
¹⁴⁷ Ba	0.890	0.022	¹⁴⁹ Ce	0.870	0.014	¹⁵¹ Nd	0.830	0.022	¹⁵⁹ Sm	0.770	0.022
¹⁴⁸ Ba	0.890	0.022	¹⁵⁰ Ce	0.870	0.014	¹⁵² Nd	0.830	0.051	¹⁶⁰ Sm	0.770	0.032
¹²⁴ La	0.440	0.200	¹⁵¹ Ce	0.850	0.022	¹⁵³ Nd	0.810	0.041	¹⁴⁷ Eu	0.660	0.051
¹²⁵ La	0.610	0.090	¹⁵² Ce	0.850	0.050	¹⁵⁴ Nd	0.800	0.051	¹⁴⁸ Eu	0.690	0.041
¹²⁶ La	0.680	0.051	¹²⁸ Pr	0.450	0.130	¹⁵⁵ Nd	0.810	0.022	¹⁴⁹ Eu	0.700	0.040
¹²⁷ La	0.700	0.041	¹²⁹ Pr	0.550	0.100	¹⁵⁶ Nd	0.820	0.014	¹⁵⁰ Eu	0.710	0.014
¹²⁸ La	0.720	0.014	¹³⁰ Pr	0.590	0.080	¹³³ Pm	0.460	0.150	¹⁵¹ Eu	0.720	0.010
¹²⁹ La	0.750	0.014	¹³¹ Pr	0.660	0.032	¹³⁴ Pm	0.520	0.120	¹⁵² Eu	0.710	0.014
¹³⁰ La	0.790	0.041	¹³² Pr	0.690	0.014	¹³⁵ Pm	0.590	0.080	¹⁵³ Eu	0.720	0.014
¹³¹ La	0.810	0.014	¹³³ Pr	0.720	0.014	¹³⁶ Pm	0.650	0.030	¹⁵⁴ Eu	0.750	0.040
¹³² La	0.840	0.014	¹³⁴ Pr	0.740	0.014	¹³⁷ Pm	0.670	0.032	¹⁵⁵ Eu	0.750	0.022
¹³³ La	0.850	0.014	¹³⁵ Pr	0.750	0.022	¹³⁸ Pm	0.700	0.028	¹⁵⁶ Eu	0.750	0.010
¹³⁴ La	0.860	0.014	¹³⁶ Pr	0.750	0.014	¹³⁹ Pm	0.690	0.030	¹⁵⁷ Eu	0.750	0.041
¹³⁵ La	0.860	0.014	¹³⁷ Pr	0.780	0.014	¹⁴⁰ Pm	0.740	0.014	¹⁴⁹ Gd	0.640	0.051
¹³⁶ La	0.870	0.014	¹³⁸ Pr	0.770	0.022	¹⁴¹ Pm	0.760	0.014	¹⁵⁰ Gd	0.640	0.041
¹³⁷ La	0.860	0.014	¹³⁹ Pr	0.790	0.014	¹⁴² Pm	0.780	0.014	¹⁵¹ Gd	0.670	0.041
¹³⁸ La	0.860	0.014	¹⁴⁰ Pr	0.810	0.014	¹⁴³ Pm	0.760	0.022	¹⁵² Gd	0.690	0.010
¹³⁹ La	0.860	0.014	¹⁴¹ Pr	0.820	0.014	¹⁴⁴ Pm	0.800	0.022	¹⁵³ Gd	0.670	0.022
¹⁴⁰ La	0.870	0.014	¹⁴² Pr	0.820	0.022	¹⁴⁵ Pm	0.770	0.022	¹⁵⁴ Gd	0.700	0.041
¹⁴¹ La	0.860	0.032	¹⁴³ Pr	0.840	0.014	¹⁴⁶ Pm	0.790	0.014	¹⁵⁵ Gd	0.700	0.014
¹⁴² La	0.870	0.014	¹⁴⁴ Pr	0.850	0.014	¹⁴⁷ Pm	0.810	0.014	¹⁵⁶ Gd	0.710	0.014
¹⁴³ La	0.870	0.014	¹⁴⁵ Pr	0.860	0.014	¹⁴⁸ Pm	0.820	0.014	¹⁵⁷ Gd	0.720	0.014
¹⁴⁴ La	0.860	0.032	¹⁴⁶ Pr	0.860	0.014	¹⁴⁹ Pm	0.830	0.014	¹⁵⁸ Gd	0.710	0.032
¹⁴⁵ La	0.880	0.014	¹⁴⁷ Pr	0.850	0.014	¹⁵⁰ Pm	0.810	0.014	¹⁵⁹ Gd	0.710	0.022
¹⁴⁶ La	0.870	0.014	¹⁴⁸ Pr	0.860	0.014	¹⁵¹ Pm	0.820	0.014	¹⁵⁴ Tb	0.680	0.032
¹⁴⁷ La	0.870	0.014	¹⁴⁹ Pr	0.840	0.022	¹⁵² Pm	0.810	0.014	¹⁵⁵ Tb	0.690	0.030
¹⁴⁸ La	0.860	0.014	¹⁵⁰ Pr	0.850	0.014	¹⁵³ Pm	0.800	0.022	¹⁵⁶ Tb	0.700	0.010
¹⁴⁹ La	0.880	0.014	¹⁵¹ Pr	0.840	0.014	¹⁵⁴ Pm	0.810	0.032	¹⁵⁷ Tb	0.700	0.010
¹⁵⁰ La	0.880	0.061	¹⁵² Pr	0.850	0.010	¹⁵⁵ Pm	0.800	0.064	¹⁵⁸ Tb	0.690	0.050
¹²⁶ Ce	0.360	0.230	¹⁵³ Pr	0.840	0.014	¹⁵⁶ Pm	0.810	0.022	¹⁵⁹ Tb	0.700	0.022
¹²⁷ Ce	0.540	0.100	¹⁵⁴ Pr	0.850	0.050	¹⁵⁷ Pm	0.810	0.014	¹⁶⁰ Tb	0.700	0.020
¹²⁸ Ce	0.660	0.030	¹³¹ Nd	0.430	0.150	¹⁵⁸ Pm	0.800	0.022	¹⁵⁶ Dy	0.660	0.061
¹²⁹ Ce	0.710	0.014	¹³² Nd	0.560	0.120	¹³⁹ Sm	0.600	0.050	¹⁵⁷ Dy	0.660	0.051
¹³⁰ Ce	0.750	0.022	¹³³ Nd	0.630	0.071	¹⁴⁰ Sm	0.630	0.060	¹⁵⁸ Dy	0.650	0.032
¹³¹ Ce	0.780	0.022	¹³⁴ Nd	0.670	0.022	¹⁴¹ Sm	0.650	0.032	¹⁵⁹ Dy	0.670	0.010
¹³² Ce	0.810	0.032	¹³⁵ Nd	0.700	0.014	¹⁴² Sm	0.690	0.022	¹⁶⁰ Dy	0.660	0.051
¹³³ Ce	0.810	0.022	¹³⁶ Nd	0.720	0.036	¹⁴³ Sm	0.710	0.022	¹⁶¹ Dy	0.670	0.010
¹³⁴ Ce	0.830	0.014	¹³⁷ Nd	0.730	0.041	¹⁴⁴ Sm	0.730	0.014	¹⁶² Dy	0.670	0.060
¹³⁵ Ce	0.840	0.014	¹³⁸ Nd	0.740	0.022	¹⁴⁵ Sm	0.730	0.014			
¹³⁶ Ce	0.840	0.014	¹³⁹ Nd	0.740	0.014	¹⁴⁶ Sm	0.740	0.014			

TABLE V. Isotopic cross sections of spallation-fission fragments of ²³⁸U(1A GeV) + d, with their statistical and systematic uncertainties.

Nucleus	σ (mb)	$\varepsilon_{\text{stat}}$ (mb)	$\varepsilon_{\text{syst}}$ (mb)	Nucleus	σ (mb)	$\varepsilon_{\text{stat}}$ (mb)	$\varepsilon_{\text{syst}}$ (mb)	Nucleus	σ (mb)	$\varepsilon_{\text{stat}}$ (mb)	$\varepsilon_{\text{syst}}$ (mb)
⁴⁹ V	0.159	0.003	0.021	⁶⁸ Ni	0.770	0.054	0.073	⁷⁵ Ge	7.405	0.142	1.637
⁵⁰ V	0.770	0.013	0.099	⁶⁹ Ni	0.437	0.032	0.090	⁷⁶ Ge	5.796	0.134	1.305
⁵¹ V	1.771	0.040	0.226	⁷⁰ Ni	0.129	0.012	0.015	⁷⁷ Ge	4.048	0.121	0.922

TABLE V. (*Continued.*)

Nucleus	σ (mb)	$\varepsilon_{\text{stat}}$ (mb)	$\varepsilon_{\text{syst}}$ (mb)	Nucleus	σ (mb)	$\varepsilon_{\text{stat}}$ (mb)	$\varepsilon_{\text{syst}}$ (mb)	Nucleus	σ (mb)	$\varepsilon_{\text{stat}}$ (mb)	$\varepsilon_{\text{syst}}$ (mb)
⁵² V	1.618	0.059	0.091	⁵⁹ Cu	0.005	0.001	0.002	⁷⁸ Ge	2.438	0.088	0.254
⁵³ V	1.470	0.074	0.083	⁶⁰ Cu	0.051	0.002	0.018	⁷⁹ Ge	1.470	0.045	0.158
⁵⁴ V	0.973	0.078	0.123	⁶¹ Cu	0.505	0.007	0.125	⁸⁰ Ge	1.255	0.034	0.277
⁵⁵ V	0.411	0.053	0.054	⁶² Cu	1.714	0.015	0.379	⁸¹ Ge	0.712	0.020	0.158
⁵⁶ V	0.219	0.037	0.032	⁶³ Cu	3.304	0.028	0.696	⁸² Ge	0.450	0.012	0.100
⁵⁷ V	0.019	0.003	0.002	⁶⁴ Cu	4.286	0.044	0.895	⁸³ Ge	0.151	0.004	0.020
⁵¹ Cr	0.375	0.005	0.059	⁶⁵ Cu	5.252	0.067	1.099	⁶⁹ As	0.053	0.001	0.013
⁵² Cr	1.333	0.017	0.202	⁶⁶ Cu	5.299	0.085	1.107	⁷⁰ As	0.481	0.006	0.109
⁵³ Cr	2.373	0.042	0.361	⁶⁷ Cu	4.369	0.089	0.932	⁷¹ As	1.600	0.014	0.359
⁵⁴ Cr	2.485	0.061	0.377	⁶⁸ Cu	3.783	0.106	0.815	⁷² As	3.586	0.030	0.801
⁵⁵ Cr	2.044	0.082	0.310	⁶⁹ Cu	2.698	0.101	0.563	⁷³ As	6.194	0.056	1.381
⁵⁶ Cr	1.331	0.074	0.202	⁷⁰ Cu	1.376	0.072	0.290	⁷⁴ As	7.688	0.079	1.715
⁵⁷ Cr	0.551	0.053	0.037	⁷¹ Cu	1.094	0.062	0.104	⁷⁵ As	10.819	0.119	2.438
⁵⁸ Cr	0.281	0.037	0.020	⁷² Cu	0.437	0.027	0.092	⁷⁶ As	10.065	0.131	2.246
⁵⁹ Cr	0.068	0.010	0.007	⁷³ Cu	0.208	0.014	0.024	⁷⁷ As	10.433	0.157	2.328
⁵³ Mn	0.536	0.007	0.094	⁷⁴ Cu	0.082	0.006	0.010	⁷⁸ As	7.783	0.151	1.738
⁵⁴ Mn	1.731	0.019	0.292	⁶² Zn	0.020	0.001	0.004	⁷⁹ As	5.915	0.138	1.374
⁵⁵ Mn	2.683	0.037	0.452	⁶³ Zn	0.308	0.004	0.069	⁸⁰ As	4.191	0.138	0.430
⁵⁶ Mn	2.725	0.056	0.463	⁶⁴ Zn	1.356	0.012	0.293	⁸¹ As	2.890	0.073	0.292
⁵⁷ Mn	2.833	0.082	0.478	⁶⁵ Zn	3.039	0.024	0.659	⁸² As	2.235	0.050	0.222
⁵⁸ Mn	1.808	0.073	0.304	⁶⁶ Zn	4.647	0.043	1.006	⁸³ As	1.688	0.038	0.377
⁵⁹ Mn	1.263	0.074	0.213	⁶⁷ Zn	6.196	0.070	1.339	⁸⁴ As	0.434	0.010	0.097
⁶⁰ Mn	0.516	0.050	0.086	⁶⁸ Zn	6.349	0.088	1.373	⁸⁵ As	0.262	0.006	0.059
⁶¹ Mn	0.283	0.029	0.048	⁶⁹ Zn	5.969	0.102	1.291	⁸⁶ As	0.131	0.004	0.017
⁶² Mn	0.076	0.010	0.008	⁷⁰ Zn	5.093	0.111	1.145	⁷¹ Se	0.031	0.001	0.009
⁵⁵ Fe	0.435	0.005	0.081	⁷¹ Zn	4.100	0.117	0.887	⁷² Se	0.329	0.004	0.085
⁵⁶ Fe	2.011	0.019	0.363	⁷² Zn	2.448	0.095	0.532	⁷³ Se	1.369	0.012	0.315
⁵⁷ Fe	2.755	0.033	0.496	⁷³ Zn	1.227	0.063	0.120	⁷⁴ Se	3.053	0.025	0.703
⁵⁸ Fe	3.539	0.056	0.639	⁷⁴ Zn	0.851	0.040	0.082	⁷⁵ Se	5.501	0.047	1.269
⁵⁹ Fe	2.779	0.064	0.530	⁷⁵ Zn	0.421	0.022	0.092	⁷⁶ Se	7.932	0.075	1.828
⁶⁰ Fe	2.529	0.079	0.457	⁷⁶ Zn	0.119	0.006	0.027	⁷⁷ Se	10.228	0.108	2.358
⁶¹ Fe	1.864	0.084	0.336	⁷⁷ Zn	0.051	0.003	0.012	⁷⁸ Se	12.497	0.136	2.879
⁶² Fe	0.875	0.059	0.158	⁷⁸ Zn	0.018	0.001	0.005	⁷⁹ Se	12.054	0.160	2.780
⁶³ Fe	0.364	0.037	0.068	⁶⁵ Ga	0.084	0.001	0.020	⁸⁰ Se	10.764	0.167	2.481
⁶⁴ Fe	0.124	0.013	0.014	⁶⁶ Ga	0.723	0.007	0.177	⁸¹ Se	8.513	0.162	1.963
⁶⁵ Fe	0.012	0.001	0.008	⁶⁷ Ga	2.460	0.020	0.537	⁸² Se	6.492	0.149	1.498
⁵⁷ Co	0.112	0.001	0.023	⁶⁸ Ga	4.325	0.039	0.923	⁸³ Se	4.949	0.124	0.520
⁵⁸ Co	1.427	0.013	0.271	⁶⁹ Ga	6.319	0.066	1.349	⁸⁴ Se	4.022	0.073	0.429
⁵⁹ Co	3.057	0.030	0.588	⁷⁰ Ga	7.708	0.094	1.654	⁸⁵ Se	3.034	0.050	0.698
⁶⁰ Co	3.476	0.047	0.670	⁷¹ Ga	8.182	0.115	1.749	⁸⁶ Se	2.200	0.040	0.509
⁶¹ Co	3.503	0.062	0.696	⁷² Ga	6.917	0.121	1.501	⁸⁷ Se	1.016	0.018	0.234
⁶² Co	3.279	0.081	0.623	⁷³ Ga	5.710	0.132	1.218	⁸⁸ Se	0.463	0.009	0.060
⁶³ Co	2.533	0.083	0.500	⁷⁴ Ga	3.891	0.120	0.831	⁸⁹ Se	0.130	0.004	0.017
⁶⁴ Co	1.800	0.087	0.342	⁷⁵ Ga	1.962	0.084	0.448	⁷³ Br	0.012	0.000	0.003
⁶⁵ Co	0.846	0.062	0.163	⁷⁶ Ga	1.663	0.065	0.159	⁷⁴ Br	0.164	0.003	0.044
⁶⁶ Co	0.386	0.030	0.073	⁷⁷ Ga	0.879	0.031	0.197	⁷⁵ Br	0.962	0.010	0.236
⁶⁷ Co	0.266	0.023	0.052	⁷⁸ Ga	0.422	0.020	0.056	⁷⁶ Br	2.496	0.021	0.581
⁶⁸ Co	0.095	0.010	0.011	⁷⁹ Ga	0.291	0.011	0.037	⁷⁷ Br	4.120	0.035	0.949
⁶⁹ Co	0.042	0.005	0.006	⁸⁰ Ga	0.119	0.005	0.014	⁷⁸ Br	7.264	0.069	1.694
⁶⁰ Ni	0.567	0.005	0.114	⁶⁷ Ge	0.073	0.001	0.018	⁷⁹ Br	10.398	0.100	2.416
⁶¹ Ni	2.768	0.025	0.559	⁶⁸ Ge	0.465	0.005	0.122	⁸⁰ Br	12.284	0.124	2.852
⁶² Ni	3.370	0.037	0.673	⁶⁹ Ge	2.159	0.018	0.515	⁸¹ Br	14.471	0.162	3.359
⁶³ Ni	4.156	0.063	0.830	⁷⁰ Ge	3.997	0.033	0.903	⁸² Br	12.041	0.163	2.797
⁶⁴ Ni	3.916	0.075	0.816	⁷¹ Ge	6.243	0.061	1.379	⁸³ Br	10.773	0.174	2.484
⁶⁵ Ni	3.886	0.096	0.774	⁷² Ge	8.447	0.090	1.868	⁸⁴ Br	8.430	0.166	1.943
⁶⁶ Ni	2.549	0.094	0.508	⁷³ Ge	9.475	0.118	2.091	⁸⁵ Br	5.936	0.153	0.705
⁶⁷ Ni	1.745	0.087	0.348	⁷⁴ Ge	8.801	0.128	1.969	⁸⁶ Br	5.630	0.103	0.591

TABLE VI. Isotopic cross sections of spallation-fission fragments of $^{238}\text{U}(1\text{A GeV}) + d$, with their statistical and systematic uncertainties.

Nucleus	σ (mb)	$\varepsilon_{\text{stat}}$ (mb)	$\varepsilon_{\text{syst}}$ (mb)	Nucleus	σ (mb)	$\varepsilon_{\text{stat}}$ (mb)	$\varepsilon_{\text{syst}}$ (mb)	Nucleus	σ (mb)	$\varepsilon_{\text{stat}}$ (mb)	$\varepsilon_{\text{syst}}$ (mb)
^{87}Br	5.336	0.078	0.548	^{94}Sr	10.720	0.125	1.122	^{97}Nb	17.958	0.199	4.131
^{88}Br	3.583	0.054	0.826	^{95}Sr	7.233	0.076	1.658	^{98}Nb	16.911	0.211	3.923
^{89}Br	2.128	0.032	0.492	^{96}Sr	5.207	0.060	1.187	^{99}Nb	16.133	0.217	3.718
^{90}Br	0.791	0.014	0.181	^{97}Sr	2.715	0.033	0.619	^{100}Nb	14.169	0.236	1.502
^{91}Br	0.317	0.006	0.040	^{98}Sr	1.344	0.018	0.306	^{101}Nb	13.049	0.170	1.411
^{92}Br	0.070	0.003	0.011	^{99}Sr	0.343	0.007	0.044	^{102}Nb	8.380	0.092	0.973
^{76}Kr	0.081	0.001	0.021	^{100}Sr	0.116	0.003	0.015	^{103}Nb	7.247	0.072	0.762
^{77}Kr	0.790	0.009	0.196	^{82}Y	0.037	0.001	0.016	^{104}Nb	3.629	0.046	0.382
^{78}Kr	2.056	0.018	0.482	^{83}Y	0.200	0.003	0.072	^{105}Nb	1.913	0.027	0.240
^{79}Kr	3.965	0.035	0.904	^{84}Y	0.825	0.010	0.200	^{106}Nb	0.634	0.012	0.079
^{80}Kr	6.672	0.059	1.532	^{85}Y	2.260	0.021	0.585	^{107}Nb	0.223	0.005	0.029
^{81}Kr	10.931	0.099	2.492	^{86}Y	5.244	0.045	1.221	^{89}Mo	0.065	0.002	0.018
^{82}Kr	13.344	0.120	3.090	^{87}Y	8.730	0.073	2.020	^{90}Mo	0.188	0.003	0.043
^{83}Kr	16.319	0.166	3.724	^{88}Y	14.169	0.116	3.286	^{91}Mo	1.132	0.012	0.314
^{84}Kr	15.467	0.183	3.549	^{89}Y	17.153	0.138	4.025	^{92}Mo	2.744	0.025	0.623
^{85}Kr	13.574	0.186	3.095	^{90}Y	18.829	0.174	4.335	^{93}Mo	5.860	0.052	1.351
^{86}Kr	10.429	0.172	2.420	^{91}Y	19.189	0.199	4.433	^{94}Mo	8.661	0.075	1.979
^{87}Kr	8.922	0.172	2.033	^{92}Y	17.069	0.200	3.926	^{95}Mo	12.761	0.106	2.951
^{88}Kr	8.752	0.173	0.917	^{93}Y	15.452	0.204	3.576	^{96}Mo	15.633	0.132	3.630
^{89}Kr	6.873	0.093	0.705	^{94}Y	14.498	0.214	3.343	^{97}Mo	18.477	0.169	4.249
^{90}Kr	5.934	0.069	1.356	^{95}Y	11.265	0.211	1.178	^{98}Mo	20.955	0.200	4.798
^{91}Kr	3.999	0.055	0.912	^{96}Y	10.508	0.141	1.308	^{99}Mo	21.074	0.213	4.799
^{92}Kr	1.925	0.025	0.440	^{97}Y	9.141	0.101	1.016	^{100}Mo	20.067	0.226	4.564
^{93}Kr	0.709	0.011	0.161	^{98}Y	6.172	0.067	1.421	^{101}Mo	18.476	0.225	4.224
^{94}Kr	0.225	0.005	0.029	^{99}Y	4.739	0.056	1.090	^{102}Mo	17.654	0.233	4.035
^{95}Kr	0.055	0.002	0.008	^{100}Y	1.918	0.025	0.441	^{103}Mo	14.549	0.240	1.532
^{78}Rb	0.037	0.001	0.009	^{101}Y	0.763	0.011	0.176	^{104}Mo	11.788	0.127	1.323
^{79}Rb	0.458	0.006	0.114	^{102}Y	0.216	0.005	0.028	^{105}Mo	7.935	0.088	0.833
^{80}Rb	1.572	0.015	0.376	^{84}Zr	0.005	0.000	0.001	^{106}Mo	5.116	0.057	0.534
^{81}Rb	3.455	0.029	0.810	^{85}Zr	0.141	0.003	0.034	^{107}Mo	2.385	0.037	0.543
^{82}Rb	6.654	0.058	1.521	^{86}Zr	0.394	0.005	0.094	^{108}Mo	1.131	0.019	0.257
^{83}Rb	10.221	0.087	2.359	^{87}Zr	1.842	0.018	0.433	^{109}Mo	0.344	0.009	0.043
^{84}Rb	14.326	0.123	3.316	^{88}Zr	3.849	0.033	0.926	^{110}Mo	0.119	0.004	0.015
^{85}Rb	17.249	0.157	4.034	^{89}Zr	8.169	0.066	1.905	^{91}Tc	0.045	0.001	0.010
^{86}Rb	17.218	0.184	3.963	^{90}Zr	12.143	0.097	2.831	^{92}Tc	0.246	0.004	0.069
^{87}Rb	15.941	0.191	3.634	^{91}Zr	16.194	0.132	3.759	^{93}Tc	0.855	0.010	0.217
^{88}Rb	12.739	0.185	2.926	^{92}Zr	17.942	0.157	4.158	^{94}Tc	2.397	0.024	0.550
^{89}Rb	11.586	0.191	2.664	^{93}Zr	18.508	0.185	4.290	^{95}Tc	4.171	0.039	0.969
^{90}Rb	9.864	0.211	1.040	^{94}Zr	18.217	0.195	4.190	^{96}Tc	6.673	0.062	1.555
^{91}Rb	8.898	0.129	0.944	^{95}Zr	17.963	0.215	4.137	^{97}Tc	9.851	0.085	2.316
^{92}Rb	7.201	0.088	0.753	^{96}Zr	15.344	0.208	3.533	^{98}Tc	14.187	0.120	3.322
^{93}Rb	5.593	0.065	1.276	^{97}Zr	14.472	0.216	3.333	^{99}Tc	16.592	0.147	3.869
^{94}Rb	3.166	0.044	0.722	^{98}Zr	13.364	0.229	1.443	^{100}Tc	19.663	0.185	4.508
^{95}Rb	1.536	0.021	0.351	^{99}Zr	11.323	0.125	1.275	^{101}Tc	20.179	0.197	4.609
^{96}Rb	0.510	0.009	0.116	^{100}Zr	9.751	0.093	1.061	^{102}Tc	18.649	0.200	4.313
^{97}Rb	0.217	0.005	0.028	^{101}Zr	5.516	0.061	0.579	^{103}Tc	21.048	0.231	4.807
^{80}Sr	0.030	0.001	0.008	^{102}Zr	3.289	0.040	0.757	^{104}Tc	17.382	0.224	3.960
^{81}Sr	0.324	0.005	0.106	^{103}Zr	1.150	0.017	0.266	^{105}Tc	16.068	0.224	3.658
^{82}Sr	0.864	0.009	0.225	^{104}Zr	0.414	0.008	0.095	^{106}Tc	11.778	0.170	1.345
^{83}Sr	2.878	0.026	0.673	^{105}Zr	0.093	0.003	0.013	^{107}Tc	10.211	0.111	1.119
^{84}Sr	5.304	0.045	1.258	^{87}Nb	0.106	0.002	0.033	^{108}Tc	5.921	0.067	0.618
^{85}Sr	9.982	0.085	2.306	^{88}Nb	0.445	0.006	0.125	^{109}Tc	3.708	0.045	0.387
^{86}Sr	13.913	0.114	3.182	^{89}Nb	1.422	0.015	0.332	^{110}Tc	1.718	0.029	0.211
^{87}Sr	17.897	0.149	4.076	^{90}Nb	3.462	0.031	0.811	^{111}Tc	0.751	0.014	0.093
^{88}Sr	18.938	0.188	4.369	^{91}Nb	7.335	0.060	1.688	^{93}Ru	0.020	0.001	0.005

TABLE VI. (*Continued.*)

Nucleus	σ (mb)	$\varepsilon_{\text{stat}}$ (mb)	$\varepsilon_{\text{syst}}$ (mb)	Nucleus	σ (mb)	$\varepsilon_{\text{stat}}$ (mb)	$\varepsilon_{\text{syst}}$ (mb)	Nucleus	σ (mb)	$\varepsilon_{\text{stat}}$ (mb)	$\varepsilon_{\text{syst}}$ (mb)
⁸⁹ Sr	18.306	0.200	4.197	⁹² Nb	10.170	0.084	2.395	⁹⁴ Ru	0.026	0.001	0.008
⁹⁰ Sr	15.109	0.195	3.445	⁹³ Nb	13.121	0.109	3.029	⁹⁵ Ru	0.583	0.008	0.136
⁹¹ Sr	13.863	0.203	3.162	⁹⁴ Nb	15.875	0.137	3.678	⁹⁶ Ru	1.588	0.018	0.394
⁹² Sr	12.004	0.200	2.739	⁹⁵ Nb	19.255	0.182	4.458	⁹⁷ Ru	3.631	0.037	0.872
⁹³ Sr	10.979	0.202	1.175	⁹⁶ Nb	18.550	0.188	4.284	⁹⁸ Ru	5.619	0.053	1.327

TABLE VII. Isotopic cross sections of spallation-fission fragments of ²³⁸U(1A GeV) + *d*, with their statistical and systematic uncertainties.

Nucleus	σ (mb)	$\varepsilon_{\text{stat}}$ (mb)	$\varepsilon_{\text{syst}}$ (mb)	Nucleus	σ (mb)	$\varepsilon_{\text{stat}}$ (mb)	$\varepsilon_{\text{syst}}$ (mb)	Nucleus	σ (mb)	$\varepsilon_{\text{stat}}$ (mb)	$\varepsilon_{\text{syst}}$ (mb)
⁹⁹ Ru	8.850	0.080	2.063	¹¹⁸ Pd	1.174	0.024	0.124	¹¹⁵ In	13.844	0.151	3.296
¹⁰⁰ Ru	12.199	0.104	2.846	¹¹⁹ Pd	0.460	0.011	0.057	¹¹⁶ In	15.444	0.171	3.592
¹⁰¹ Ru	16.912	0.148	3.880	¹²⁰ Pd	0.136	0.005	0.019	¹¹⁷ In	15.690	0.178	3.638
¹⁰² Ru	18.222	0.165	4.239	¹⁰⁰ Ag	0.012	0.000	0.002	¹¹⁸ In	14.787	0.183	3.407
¹⁰³ Ru	19.590	0.189	4.497	¹⁰¹ Ag	0.076	0.002	0.019	¹¹⁹ In	13.862	0.176	3.192
¹⁰⁴ Ru	19.782	0.198	4.625	¹⁰² Ag	0.471	0.007	0.113	¹²⁰ In	12.203	0.159	2.811
¹⁰⁵ Ru	19.489	0.211	4.523	¹⁰³ Ag	1.229	0.016	0.282	¹²¹ In	10.288	0.166	1.109
¹⁰⁶ Ru	19.459	0.229	4.438	¹⁰⁴ Ag	2.326	0.026	0.574	¹²² In	8.373	0.117	0.947
¹⁰⁷ Ru	17.368	0.224	3.954	¹⁰⁵ Ag	3.769	0.040	0.969	¹²³ In	6.136	0.080	0.694
¹⁰⁸ Ru	15.723	0.232	1.703	¹⁰⁶ Ag	6.369	0.062	1.491	¹²⁴ In	3.472	0.047	0.378
¹⁰⁹ Ru	10.755	0.134	1.212	¹⁰⁷ Ag	9.757	0.092	2.382	¹²⁵ In	1.783	0.027	0.191
¹¹⁰ Ru	8.438	0.096	0.963	¹⁰⁸ Ag	12.643	0.120	2.950	¹²⁶ In	0.968	0.020	0.103
¹¹¹ Ru	4.769	0.057	0.497	¹⁰⁹ Ag	15.100	0.143	3.501	¹²⁷ In	0.548	0.012	0.068
¹¹² Ru	2.682	0.039	0.334	¹¹⁰ Ag	16.290	0.165	3.756	¹²⁸ In	0.038	0.001	0.009
¹¹³ Ru	1.017	0.021	0.125	¹¹¹ Ag	18.021	0.183	4.161	¹⁰⁷ Sn	0.008	0.001	0.002
¹¹⁴ Ru	0.437	0.011	0.053	¹¹² Ag	17.368	0.192	3.998	¹⁰⁸ Sn	0.034	0.001	0.009
¹¹⁵ Ru	0.122	0.004	0.015	¹¹³ Ag	17.722	0.203	4.065	¹⁰⁹ Sn	0.281	0.006	0.064
⁹⁶ Rh	0.030	0.001	0.013	¹¹⁴ Ag	16.645	0.205	3.794	¹¹⁰ Sn	0.727	0.011	0.177
⁹⁷ Rh	0.268	0.004	0.101	¹¹⁵ Ag	15.805	0.194	3.593	¹¹¹ Sn	1.822	0.023	0.440
⁹⁸ Rh	1.005	0.012	0.240	¹¹⁶ Ag	12.694	0.194	1.481	¹¹² Sn	2.825	0.033	0.735
⁹⁹ Rh	2.145	0.023	0.540	¹¹⁷ Ag	9.756	0.115	1.180	¹¹³ Sn	4.408	0.051	1.103
¹⁰⁰ Rh	4.265	0.043	0.981	¹¹⁸ Ag	6.062	0.074	0.685	¹¹⁴ Sn	6.598	0.073	1.689
¹⁰¹ Rh	6.882	0.064	1.586	¹¹⁹ Ag	3.861	0.048	0.410	¹¹⁵ Sn	8.391	0.091	2.113
¹⁰² Rh	10.234	0.092	2.376	¹²⁰ Ag	1.616	0.026	0.174	¹¹⁶ Sn	9.622	0.105	2.406
¹⁰³ Rh	14.602	0.126	3.401	¹²¹ Ag	0.809	0.017	0.098	¹¹⁷ Sn	11.996	0.134	2.826
¹⁰⁴ Rh	17.064	0.157	3.942	¹²² Ag	0.264	0.008	0.034	¹¹⁸ Sn	11.668	0.134	2.781
¹⁰⁵ Rh	20.457	0.189	4.716	¹⁰³ Cd	0.019	0.001	0.005	¹¹⁹ Sn	12.795	0.150	3.035
¹⁰⁶ Rh	19.515	0.196	4.499	¹⁰⁴ Cd	0.254	0.005	0.061	¹²⁰ Sn	12.038	0.156	2.769
¹⁰⁷ Rh	20.153	0.206	4.611	¹⁰⁵ Cd	0.843	0.012	0.280	¹²¹ Sn	12.193	0.159	2.814
¹⁰⁸ Rh	18.780	0.215	4.298	¹⁰⁶ Cd	1.709	0.021	0.462	¹²² Sn	11.054	0.146	2.555
¹⁰⁹ Rh	16.913	0.202	4.612	¹⁰⁷ Cd	3.123	0.034	0.781	¹²³ Sn	9.376	0.136	1.003
¹¹⁰ Rh	15.025	0.200	1.576	¹⁰⁸ Cd	4.959	0.052	1.283	¹²⁴ Sn	7.555	0.127	0.867
¹¹¹ Rh	13.508	0.197	1.593	¹⁰⁹ Cd	7.643	0.076	1.795	¹²⁵ Sn	5.881	0.078	0.682
¹¹² Rh	10.379	0.120	1.238	¹¹⁰ Cd	9.638	0.095	2.276	¹²⁶ Sn	3.669	0.049	0.413
¹¹³ Rh	6.707	0.076	0.795	¹¹¹ Cd	12.226	0.120	2.817	¹²⁷ Sn	2.771	0.036	0.297
¹¹⁴ Rh	3.412	0.044	0.359	¹¹² Cd	14.366	0.145	3.283	¹²⁸ Sn	1.820	0.026	0.196
¹¹⁵ Rh	1.745	0.030	0.215	¹¹³ Cd	15.128	0.160	3.435	¹²⁹ Sn	1.343	0.019	0.166
¹¹⁶ Rh	0.685	0.015	0.083	¹¹⁴ Cd	15.777	0.171	3.600	¹³⁰ Sn	1.169	0.014	0.144
¹¹⁷ Rh	0.251	0.007	0.032	¹¹⁵ Cd	16.475	0.190	3.731	¹³¹ Sn	0.733	0.008	0.091
¹¹⁸ Rh	0.070	0.003	0.010	¹¹⁶ Cd	16.740	0.203	3.761	¹³² Sn	0.442	0.006	0.055
⁹⁸ Pd	0.002	0.000	0.000	¹¹⁷ Cd	15.113	0.190	3.410	¹³³ Sn	0.012	0.000	0.004
⁹⁹ Pd	0.191	0.004	0.054	¹¹⁸ Cd	10.934	0.156	2.513	¹⁰⁹ Sb	0.009	0.001	0.002

TABLE VII. (Continued.)

Nucleus	σ (mb)	ϵ_{stat} (mb)	ϵ_{syst} (mb)	Nucleus	σ (mb)	ϵ_{stat} (mb)	ϵ_{syst} (mb)	Nucleus	σ (mb)	ϵ_{stat} (mb)	ϵ_{syst} (mb)
¹⁰⁰ Pd	0.727	0.010	0.175	¹¹⁹ Cd	10.290	0.153	1.115	¹¹⁰ Sb	0.057	0.002	0.014
¹⁰¹ Pd	1.862	0.022	0.485	¹²⁰ Cd	7.704	0.096	0.801	¹¹¹ Sb	0.168	0.005	0.042
¹⁰² Pd	3.455	0.037	0.854	¹²¹ Cd	4.621	0.059	0.562	¹¹² Sb	0.570	0.010	0.139
¹⁰³ Pd	5.816	0.057	1.394	¹²² Cd	2.467	0.035	0.257	¹¹³ Sb	1.178	0.017	0.295
¹⁰⁴ Pd	8.667	0.080	2.125	¹²³ Cd	1.327	0.026	0.140	¹¹⁴ Sb	2.131	0.029	0.513
¹⁰⁵ Pd	11.983	0.108	2.835	¹²⁴ Cd	0.510	0.012	0.062	¹¹⁵ Sb	3.333	0.040	0.842
¹⁰⁶ Pd	14.443	0.134	3.394	¹²⁵ Cd	0.203	0.006	0.025	¹¹⁶ Sb	5.252	0.062	1.347
¹⁰⁷ Pd	17.980	0.167	4.203	¹²⁶ Cd	0.077	0.003	0.010	¹¹⁷ Sb	6.393	0.077	1.650
¹⁰⁸ Pd	19.669	0.194	4.581	¹⁰⁵ In	0.013	0.000	0.003	¹¹⁸ Sb	8.164	0.094	2.079
¹⁰⁹ Pd	19.397	0.198	4.516	¹⁰⁶ In	0.114	0.003	0.029	¹¹⁹ Sb	9.653	0.114	2.350
¹¹⁰ Pd	18.034	0.198	4.195	¹⁰⁷ In	0.452	0.008	0.118	¹²⁰ Sb	10.961	0.132	2.603
¹¹¹ Pd	17.787	0.212	4.109	¹⁰⁸ In	1.084	0.015	0.265	¹²¹ Sb	11.627	0.143	2.747
¹¹² Pd	17.657	0.215	4.071	¹⁰⁹ In	2.088	0.025	0.503	¹²² Sb	11.060	0.144	2.570
¹¹³ Pd	14.161	0.202	2.715	¹¹⁰ In	3.877	0.042	0.975	¹²³ Sb	11.611	0.156	2.688
¹¹⁴ Pd	10.619	0.139	1.200	¹¹¹ In	5.395	0.055	1.385	¹²⁴ Sb	10.784	0.147	2.481
¹¹⁵ Pd	7.617	0.092	0.918	¹¹² In	7.881	0.082	2.007	¹²⁵ Sb	9.661	0.134	2.221
¹¹⁶ Pd	4.432	0.053	0.509	¹¹³ In	10.381	0.105	2.550	¹²⁶ Sb	7.116	0.119	1.633
¹¹⁷ Pd	2.208	0.032	0.233	¹¹⁴ In	12.574	0.130	2.968	¹²⁷ Sb	6.640	0.104	0.716

TABLE VIII. Isotopic cross sections of spallation-fission fragments of ²³⁸U(1A GeV) + *d*, with their statistical and systematic uncertainties.

Nucleus	σ (mb)	ϵ_{stat} (mb)	ϵ_{syst} (mb)	Nucleus	σ (mb)	ϵ_{stat} (mb)	ϵ_{syst} (mb)	Nucleus	σ (mb)	ϵ_{stat} (mb)	ϵ_{syst} (mb)
¹²⁸ Sb	5.094	0.068	0.579	¹³⁹ I	0.139	0.002	0.034	¹²³ Ba	0.199	0.005	0.049
¹²⁹ Sb	3.929	0.047	0.423	¹⁴⁰ I	0.035	0.001	0.009	¹²⁴ Ba	0.397	0.009	0.127
¹³⁰ Sb	3.203	0.037	0.344	¹⁴¹ I	0.011	0.000	0.003	¹²⁵ Ba	0.822	0.016	0.225
¹³¹ Sb	3.059	0.034	0.703	¹¹⁷ Xe	0.042	0.002	0.009	¹²⁶ Ba	1.120	0.019	0.375
¹³² Sb	2.227	0.023	0.274	¹¹⁸ Xe	0.131	0.004	0.030	¹²⁷ Ba	1.750	0.029	0.525
¹³³ Sb	1.720	0.017	0.212	¹¹⁹ Xe	0.403	0.009	0.101	¹²⁸ Ba	2.072	0.036	0.713
¹³⁴ Sb	0.096	0.001	0.026	¹²⁰ Xe	0.920	0.015	0.222	¹²⁹ Ba	2.707	0.046	0.874
¹³⁵ Sb	0.029	0.001	0.009	¹²¹ Xe	1.578	0.024	0.455	¹³⁰ Ba	2.968	0.052	0.975
¹¹² Te	0.024	0.001	0.007	¹²² Xe	2.034	0.030	0.581	¹³¹ Ba	3.550	0.063	0.975
¹¹³ Te	0.115	0.003	0.027	¹²³ Xe	2.824	0.043	0.797	¹³² Ba	3.919	0.074	1.053
¹¹⁴ Te	0.329	0.007	0.079	¹²⁴ Xe	3.999	0.059	1.067	¹³³ Ba	3.899	0.079	0.966
¹¹⁵ Te	0.841	0.014	0.205	¹²⁵ Xe	5.219	0.076	1.345	¹³⁴ Ba	4.302	0.085	1.063
¹¹⁶ Te	1.537	0.021	0.387	¹²⁶ Xe	4.898	0.074	1.363	¹³⁵ Ba	3.729	0.077	0.873
¹¹⁷ Te	2.559	0.034	0.620	¹²⁷ Xe	6.186	0.096	1.540	¹³⁶ Ba	3.508	0.071	0.825
¹¹⁸ Te	3.488	0.046	0.910	¹²⁸ Xe	6.546	0.104	1.606	¹³⁷ Ba	3.654	0.073	0.839
¹¹⁹ Te	4.839	0.063	1.246	¹²⁹ Xe	6.572	0.108	1.576	¹³⁸ Ba	3.739	0.073	0.854
¹²⁰ Te	6.182	0.077	1.655	¹³⁰ Xe	6.786	0.114	1.612	¹³⁹ Ba	3.354	0.075	0.364
¹²¹ Te	6.582	0.086	1.664	¹³¹ Xe	6.535	0.109	1.541	¹⁴⁰ Ba	3.744	0.071	0.405
¹²² Te	8.342	0.110	2.066	¹³² Xe	6.230	0.105	1.432	¹⁴¹ Ba	3.508	0.049	0.381
¹²³ Te	9.281	0.127	2.194	¹³³ Xe	5.988	0.100	0.647	¹⁴² Ba	3.914	0.044	0.426
¹²⁴ Te	8.650	0.124	2.087	¹³⁴ Xe	5.450	0.107	0.601	¹⁴³ Ba	3.240	0.033	0.352
¹²⁵ Te	9.477	0.139	2.215	¹³⁵ Xe	6.154	0.088	0.668	¹⁴⁴ Ba	2.517	0.024	0.303
¹²⁶ Te	9.294	0.137	2.143	¹³⁶ Xe	6.596	0.073	0.755	¹⁴⁵ Ba	0.755	0.010	0.174
¹²⁷ Te	8.778	0.128	2.022	¹³⁷ Xe	5.196	0.052	0.562	¹⁴⁶ Ba	0.350	0.006	0.081
¹²⁸ Te	6.930	0.106	0.761	¹³⁸ Xe	4.648	0.041	0.500	¹⁴⁷ Ba	0.060	0.001	0.016
¹²⁹ Te	6.561	0.122	0.717	¹³⁹ Xe	2.848	0.027	0.309	¹⁴⁸ Ba	0.014	0.001	0.004
¹³⁰ Te	5.171	0.071	0.557	¹⁴⁰ Xe	2.108	0.022	0.256	¹²⁴ La	0.037	0.002	0.013

TABLE VIII. (*Continued.*)

Nucleus	σ (mb)	$\varepsilon_{\text{stat}}$ (mb)	$\varepsilon_{\text{syst}}$ (mb)	Nucleus	σ (mb)	$\varepsilon_{\text{stat}}$ (mb)	$\varepsilon_{\text{syst}}$ (mb)	Nucleus	σ (mb)	$\varepsilon_{\text{stat}}$ (mb)	$\varepsilon_{\text{syst}}$ (mb)
¹³¹ Te	4.740	0.057	0.549	¹⁴¹ Xe	1.030	0.013	0.128	¹²⁵ La	0.110	0.003	0.027
¹³² Te	4.721	0.047	0.531	¹⁴² Xe	0.071	0.001	0.019	¹²⁶ La	0.307	0.008	0.082
¹³³ Te	4.802	0.041	0.518	¹⁴³ Xe	0.015	0.000	0.005	¹²⁷ La	0.530	0.011	0.164
¹³⁴ Te	4.534	0.040	0.557	¹¹⁹ Cs	0.022	0.001	0.005	¹²⁸ La	1.043	0.019	0.274
¹³⁵ Te	2.009	0.020	0.247	¹²⁰ Cs	0.088	0.003	0.021	¹²⁹ La	1.136	0.022	0.422
¹³⁶ Te	0.202	0.002	0.051	¹²¹ Cs	0.258	0.006	0.065	¹³⁰ La	1.520	0.029	0.584
¹³⁷ Te	0.075	0.001	0.021	¹²² Cs	0.630	0.012	0.153	¹³¹ La	1.771	0.035	0.611
¹³⁸ Te	0.023	0.001	0.006	¹²³ Cs	1.102	0.019	0.288	¹³² La	2.417	0.046	0.719
¹³⁹ Te	0.004	0.000	0.001	¹²⁴ Cs	1.756	0.028	0.467	¹³³ La	2.447	0.050	0.718
¹¹⁵ I	0.064	0.003	0.013	¹²⁵ Cs	2.181	0.034	0.646	¹³⁴ La	2.842	0.058	0.797
¹¹⁶ I	0.183	0.005	0.047	¹²⁶ Cs	3.203	0.050	0.937	¹³⁵ La	2.759	0.061	0.731
¹¹⁷ I	0.602	0.012	0.138	¹²⁷ Cs	3.385	0.054	1.040	¹³⁶ La	2.811	0.065	0.683
¹¹⁸ I	1.204	0.020	0.312	¹²⁸ Cs	4.366	0.068	1.172	¹³⁷ La	2.652	0.062	0.622
¹¹⁹ I	2.044	0.029	0.547	¹²⁹ Cs	4.306	0.070	1.169	¹³⁸ La	2.456	0.058	0.564
¹²⁰ I	3.138	0.044	0.816	¹³⁰ Cs	5.149	0.088	1.244	¹³⁹ La	2.583	0.059	0.592
¹²¹ I	4.010	0.056	1.004	¹³¹ Cs	4.911	0.087	1.187	¹⁴⁰ La	2.078	0.054	0.474
¹²² I	5.062	0.069	1.332	¹³² Cs	4.952	0.090	1.166	¹⁴¹ La	1.842	0.046	0.199
¹²³ I	5.559	0.076	1.501	¹³³ Cs	4.893	0.089	1.131	¹⁴² La	2.120	0.058	0.232
¹²⁴ I	6.889	0.098	1.682	¹³⁴ Cs	4.654	0.084	1.065	¹⁴³ La	2.106	0.042	0.230
¹²⁵ I	7.440	0.109	1.822	¹³⁵ Cs	4.548	0.082	1.046	¹⁴⁴ La	1.937	0.034	0.217
¹²⁶ I	8.073	0.116	1.893	¹³⁶ Cs	4.116	0.077	0.455	¹⁴⁵ La	2.074	0.028	0.248
¹²⁷ I	7.588	0.115	1.784	¹³⁷ Cs	4.331	0.084	0.510	¹⁴⁶ La	1.200	0.017	0.144
¹²⁸ I	7.208	0.115	1.652	¹³⁸ Cs	3.844	0.056	0.423	¹⁴⁷ La	1.175	0.017	0.142
¹²⁹ I	7.704	0.117	1.782	¹³⁹ Cs	3.495	0.042	0.407	¹⁴⁸ La	0.458	0.010	0.056
¹³⁰ I	7.240	0.114	1.665	¹⁴⁰ Cs	3.494	0.036	0.379	¹⁴⁹ La	0.059	0.002	0.014
¹³¹ I	5.971	0.106	0.644	¹⁴¹ Cs	3.116	0.029	0.338	¹⁵⁰ La	0.013	0.001	0.004
¹³² I	5.263	0.095	0.576	¹⁴² Cs	1.978	0.022	0.215	¹²⁶ Ce	0.023	0.001	0.006
¹³³ I	5.618	0.071	0.643	¹⁴³ Cs	0.648	0.008	0.150	¹²⁷ Ce	0.086	0.003	0.020
¹³⁴ I	5.121	0.055	0.572	¹⁴⁴ Cs	0.122	0.002	0.031	¹²⁸ Ce	0.233	0.006	0.067
¹³⁵ I	5.569	0.048	0.599	¹⁴⁵ Cs	0.035	0.001	0.009	¹²⁹ Ce	0.602	0.013	0.153
¹³⁶ I	3.343	0.033	0.361	¹⁴⁶ Cs	0.008	0.000	0.002	¹³⁰ Ce	0.794	0.016	0.307
¹³⁷ I	2.724	0.029	0.333	¹²¹ Ba	0.016	0.001	0.004	¹³¹ Ce	1.213	0.023	0.435
¹³⁸ I	1.472	0.017	0.181	¹²² Ba	0.064	0.002	0.014	¹³² Ce	1.181	0.024	0.638

TABLE IX. Isotopic cross sections of spallation-fission fragments of ²³⁸U(1A GeV) + *d*, with their statistical and systematic uncertainties.

Nucleus	σ (mb)	$\varepsilon_{\text{stat}}$ (mb)	$\varepsilon_{\text{syst}}$ (mb)	Nucleus	σ (mb)	$\varepsilon_{\text{stat}}$ (mb)	$\varepsilon_{\text{syst}}$ (mb)	Nucleus	σ (mb)	$\varepsilon_{\text{stat}}$ (mb)	$\varepsilon_{\text{syst}}$ (mb)
¹³³ Ce	1.627	0.032	0.646	¹⁴⁵ Nd	0.951	0.035	0.220	¹⁵⁵ Eu	0.194	0.014	0.043
¹³⁴ Ce	1.716	0.036	0.707	¹⁴⁶ Nd	0.813	0.033	0.193	¹⁵⁶ Eu	0.185	0.014	0.040
¹³⁵ Ce	1.887	0.040	0.718	¹⁴⁷ Nd	0.696	0.031	0.168	¹⁵⁷ Eu	0.087	0.009	0.019
¹³⁶ Ce	1.793	0.041	0.675	¹⁴⁸ Nd	0.666	0.030	0.163	¹⁵⁸ Eu	0.044	0.006	0.010
¹³⁷ Ce	2.280	0.054	0.602	¹⁴⁹ Nd	0.568	0.025	0.130	¹⁵⁹ Eu	0.031	0.004	0.007
¹³⁸ Ce	2.204	0.055	0.564	¹⁵⁰ Nd	0.481	0.023	0.052	¹⁶⁰ Eu	0.014	0.002	0.003
¹³⁹ Ce	2.127	0.054	0.508	¹⁵¹ Nd	0.550	0.022	0.058	¹⁵³ Gd	0.316	0.018	0.095
¹⁴⁰ Ce	2.109	0.054	0.499	¹⁵² Nd	0.358	0.014	0.038	¹⁵⁴ Gd	0.201	0.014	0.090
¹⁴¹ Ce	1.774	0.049	0.403	¹⁵³ Nd	0.262	0.011	0.029	¹⁵⁵ Gd	0.231	0.016	0.065
¹⁴² Ce	1.470	0.046	0.336	¹⁵⁴ Nd	0.141	0.007	0.020	¹⁵⁶ Gd	0.164	0.013	0.044
¹⁴³ Ce	1.369	0.039	0.358	¹⁵⁵ Nd	0.076	0.005	0.010	¹⁵⁷ Gd	0.149	0.014	0.033
¹⁴⁴ Ce	1.251	0.038	0.137	¹⁵⁶ Nd	0.005	0.001	0.001	¹⁵⁸ Gd	0.092	0.011	0.020
¹⁴⁵ Ce	1.506	0.046	0.169	¹³³ Pm	0.027	0.002	0.007	¹⁵⁹ Gd	0.079	0.009	0.017
¹⁴⁶ Ce	1.496	0.033	0.167	¹³⁴ Pm	0.069	0.003	0.018	¹⁶⁰ Gd	0.042	0.005	0.009
¹⁴⁷ Ce	1.373	0.027	0.151	¹³⁵ Pm	0.181	0.006	0.060	¹⁶¹ Gd	0.017	0.003	0.004

TABLE IX. (Continued.)

Nucleus	σ (mb)	ϵ_{stat} (mb)	ϵ_{syst} (mb)	Nucleus	σ (mb)	ϵ_{stat} (mb)	ϵ_{syst} (mb)	Nucleus	σ (mb)	ϵ_{stat} (mb)	ϵ_{syst} (mb)
¹⁴⁸ Ce	1.083	0.019	0.118	¹³⁶ Pm	0.410	0.012	0.142	¹⁶² Gd	0.009	0.002	0.002
¹⁴⁹ Ce	0.763	0.015	0.083	¹³⁷ Pm	0.516	0.014	0.262	¹⁵² Tb	0.098	0.002	0.037
¹⁵⁰ Ce	0.463	0.011	0.056	¹³⁸ Pm	0.909	0.022	0.393	¹⁵³ Tb	0.131	0.004	0.038
¹⁵¹ Ce	0.043	0.002	0.011	¹³⁹ Pm	0.634	0.018	0.555	¹⁵⁴ Tb	0.168	0.005	0.037
¹⁵² Ce	0.015	0.001	0.005	¹⁴⁰ Pm	0.843	0.022	0.630	¹⁵⁵ Tb	0.165	0.006	0.023
¹²⁸ Pr	0.023	0.002	0.005	¹⁴¹ Pm	0.469	0.016	0.413	¹⁵⁶ Tb	0.183	0.011	0.020
¹²⁹ Pr	0.052	0.002	0.013	¹⁴² Pm	0.979	0.028	0.560	¹⁵⁷ Tb	0.184	0.008	0.017
¹³⁰ Pr	0.129	0.004	0.052	¹⁴³ Pm	0.774	0.024	0.499	¹⁵⁸ Tb	0.162	0.009	0.014
¹³¹ Pr	0.349	0.009	0.097	¹⁴⁴ Pm	0.870	0.030	0.341	¹⁵⁹ Tb	0.100	0.009	0.009
¹³² Pr	0.623	0.014	0.203	¹⁴⁵ Pm	0.830	0.032	0.242	¹⁶⁰ Tb	0.067	0.005	0.006
¹³³ Pr	0.882	0.019	0.353	¹⁴⁶ Pm	0.792	0.031	0.215	¹⁶¹ Tb	0.022	0.007	0.003
¹³⁴ Pr	1.145	0.024	0.454	¹⁴⁷ Pm	0.777	0.031	0.188	¹⁵⁴ Dy	0.041	0.001	0.019
¹³⁵ Pr	0.962	0.022	0.582	¹⁴⁸ Pm	0.606	0.027	0.143	¹⁵⁵ Dy	0.088	0.002	0.031
¹³⁶ Pr	1.330	0.030	0.571	¹⁴⁹ Pm	0.511	0.024	0.114	¹⁵⁶ Dy	0.123	0.004	0.029
¹³⁷ Pr	1.160	0.029	0.584	¹⁵⁰ Pm	0.499	0.024	0.110	¹⁵⁷ Dy	0.153	0.005	0.026
¹³⁸ Pr	1.365	0.034	0.534	¹⁵¹ Pm	0.484	0.025	0.108	¹⁵⁸ Dy	0.144	0.008	0.017
¹³⁹ Pr	1.419	0.038	0.474	¹⁵² Pm	0.336	0.020	0.074	¹⁵⁹ Dy	0.151	0.006	0.014
¹⁴⁰ Pr	1.859	0.049	0.484	¹⁵³ Pm	0.326	0.020	0.037	¹⁶⁰ Dy	0.140	0.008	0.012
¹⁴¹ Pr	1.616	0.046	0.397	¹⁵⁴ Pm	0.254	0.016	0.028	¹⁶¹ Dy	0.120	0.010	0.010
¹⁴² Pr	1.447	0.044	0.342	¹⁵⁵ Pm	0.172	0.012	0.018	¹⁶² Dy	0.064	0.005	0.006
¹⁴³ Pr	1.290	0.042	0.305	¹⁵⁶ Pm	0.094	0.007	0.010	¹⁶³ Dy	0.037	0.005	0.003
¹⁴⁴ Pr	1.209	0.042	0.278	¹⁵⁷ Pm	0.007	0.001	0.002	¹⁵⁵ Ho	0.086	0.002	0.056
¹⁴⁵ Pr	1.192	0.042	0.273	¹⁵⁸ Pm	0.003	0.001	0.001	¹⁵⁶ Ho	0.126	0.003	0.066
¹⁴⁶ Pr	1.046	0.036	0.114	¹⁴⁵ Sm	0.619	0.022	0.401	¹⁵⁷ Ho	0.167	0.004	0.067
¹⁴⁷ Pr	0.835	0.033	0.092	¹⁴⁶ Sm	0.448	0.017	0.356	¹⁵⁸ Ho	0.182	0.005	0.049
¹⁴⁸ Pr	0.794	0.029	0.088	¹⁴⁷ Sm	0.620	0.025	0.196	¹⁵⁹ Ho	0.190	0.006	0.035
¹⁴⁹ Pr	0.819	0.023	0.091	¹⁴⁸ Sm	0.489	0.022	0.158	¹⁶⁰ Ho	0.152	0.008	0.018
¹⁵⁰ Pr	0.725	0.020	0.080	¹⁴⁹ Sm	0.623	0.028	0.146	¹⁶¹ Ho	0.148	0.006	0.015
¹⁵¹ Pr	0.563	0.015	0.062	¹⁵⁰ Sm	0.420	0.020	0.109	¹⁶² Ho	0.109	0.007	0.010
¹⁵² Pr	0.210	0.007	0.023	¹⁵¹ Sm	0.336	0.018	0.084	¹⁶³ Ho	0.099	0.009	0.009
¹⁵³ Pr	0.099	0.005	0.012	¹⁵² Sm	0.362	0.020	0.096	¹⁶⁴ Ho	0.062	0.005	0.005
¹⁵⁴ Pr	0.008	0.001	0.003	¹⁵³ Sm	0.276	0.017	0.076	¹⁶⁵ Ho	0.038	0.005	0.003
¹³¹ Nd	0.033	0.002	0.013	¹⁵⁴ Sm	0.233	0.016	0.057	¹⁶¹ Er	0.043	0.001	0.012
¹³² Nd	0.080	0.003	0.038	¹⁵⁵ Sm	0.153	0.013	0.037	¹⁶² Er	0.065	0.003	0.011
¹³³ Nd	0.254	0.007	0.095	¹⁵⁶ Sm	0.114	0.010	0.026	¹⁶³ Er	0.082	0.003	0.010
¹³⁴ Nd	0.450	0.011	0.210	¹⁵⁷ Sm	0.050	0.005	0.012	¹⁶⁴ Er	0.074	0.006	0.007
¹³⁵ Nd	0.662	0.016	0.346	¹⁵⁸ Sm	0.033	0.004	0.009	¹⁶⁵ Er	0.059	0.009	0.005
¹³⁶ Nd	0.906	0.021	0.458	¹⁵⁹ Sm	0.018	0.003	0.006	¹⁶⁶ Er	0.043	0.005	0.004
¹³⁷ Nd	0.988	0.023	0.593	¹⁶⁰ Sm	0.009	0.002	0.004	¹⁶⁷ Er	0.023	0.004	0.002
¹³⁸ Nd	0.992	0.025	0.656	¹⁴⁸ Eu	0.419	0.020	0.308	¹⁶⁵ Tm	0.005	0.000	0.001
¹³⁹ Nd	1.061	0.028	0.560	¹⁴⁹ Eu	0.437	0.021	0.229	¹⁶⁶ Tm	0.032	0.002	0.004
¹⁴⁰ Nd	0.867	0.026	0.598	¹⁵⁰ Eu	0.433	0.022	0.144	¹⁶⁷ Tm	0.049	0.005	0.004
¹⁴¹ Nd	1.143	0.033	0.431	¹⁵¹ Eu	0.336	0.019	0.107	¹⁶⁸ Tm	0.047	0.006	0.004
¹⁴² Nd	1.145	0.035	0.363	¹⁵² Eu	0.372	0.021	0.089	¹⁶⁹ Tm	0.028	0.004	0.003
¹⁴³ Nd	1.182	0.039	0.297	¹⁵³ Eu	0.300	0.019	0.074				
¹⁴⁴ Nd	1.034	0.037	0.244	¹⁵⁴ Eu	0.314	0.021	0.067				

- [1] RNB VI, Nucl. Phys. **A748** (2005).
- [2] The European Spallation Source Study, The ESS Technical Study, Vol. III, Report ESS-96-53-M, 1996.
- [3] C. D. Bowman, E. D. Arthur, P. W. Lisowski, G. P. Lawrence, R. J. Jensen, J. L. Anderson, B. Blind, M. Cappiello, J. W. Davidson, T. R. England, L. N. Engel, R. C. Gaight, H. G. Hughes, J. R. Ireland, R. A. Krakowski, R. J. LaBauve, B. C. Letellier, R. T. Perry, G. J. Russel, K. P. Staudhammer, G. Versamis, and W. B. Wilson, Nucl. Instrum. Methods A **320**, 336 (1992).
- [4] W. F. Henning, Nucl. Instrum. Methods B **126**, 1 (1997).
- [5] R. Michel, I. Leya, and L. Borges, Nucl. Instrum. Methods B **113**, 343 (1996).
- [6] J. Pereira, Ph.D. thesis, Universidade de Santiago de Compostela, 2004.
- [7] J. Benlliure, P. Armbruster, M. Bernas, A. Boudard, T. Enqvist, R. Legrain, S. Leray, F. Rejmund, K.-H. Schmidt, C. Stéphan, L. Tassan-Got, and C. Volant, Nucl. Phys. **A700**, 469 (2002).
- [8] P. Napolitani, K.-H. Schmidt, A. S. Botvina, F. Rejmund, L. Tassan-Got, and C. Villagrasa, Phys. Rev. C **70**, 054607 (2004).
- [9] K.-H. Schmidt, M. V. Ricciardi, A. Botvina, and T. Enqvist, Nucl. Phys. **A710**, 157 (2002).
- [10] A. R. Junghans, M. de Jong, H.-G. Clerc, A. V. Ignatyuk, G. A. Kudyaev, and K.-H. Schmidt, Nucl. Phys. **A629**, 635 (1998).
- [11] J. Pereira, P. Armbruster, J. Benlliure, M. Bernas, A. Boudard, E. Casarejos, S. Czajkowski, T. Enqvist, R. Legrain, S. Leray, B. Mustapha, M. Pravikoff, F. Rejmund, K.-H. Schmidt, C. Stéphan, J. Taïeb, L. Tassan-Got, C. Volant, and W. Wlazlo, Nucl. Phys. **A734**, 221 (2004).
- [12] E. Casarejos, J. Benlliure, J. Pereira, P. Armbruster, M. Bernas, A. Boudard, S. Czajkowski, T. Enqvist, R. Legrain, S. Leray, B. Mustapha, M. Pravikoff, F. Rejmund, K.-H. Schmidt, C. Stéphan, J. Taïeb, L. Tassan-Got, C. Volant, and W. Wlazlo, Phys. Rev. C **74**, 044612 (2006).
- [13] W. Wlazlo, T. Enqvist, P. Armbruster, J. Benlliure, M. Bernas, A. Boudard, S. Czajkowski, R. Legrain, S. Leray, B. Mustapha, M. Pravikoff, F. Rejmund, K.-H. Schmidt, C. Stéphan, J. Taïeb, L. Tassan-Got, and C. Volant, Phys. Rev. Lett. **84**, 5736 (2000).
- [14] J. Benlliure, P. Armbruster, M. Bernas, A. Boudard, J. P. Dufour, T. Enqvist, R. Legrain, S. Leray, B. Mustapha, F. Rejmund, K.-H. Schmidt, C. Stéphan, L. Tassan-Got, and C. Volant, Nucl. Phys. **A683**, 513 (2001).
- [15] F. Rejmund, B. Mustapha, P. Armbruster, J. Benlliure, M. Bernas, A. Boudard, J. P. Dufour, T. Enqvist, R. Legrain, S. Leray, M. Pravikoff, F. Rejmund, K.-H. Schmidt, C. Stéphan, J. Taïeb, L. Tassan-Got, C. Volant, and W. Wlazlo, Nucl. Phys. **A683**, 540 (2001).
- [16] T. Enqvist, W. Wlazlo, P. Armbruster, J. Benlliure, M. Bernas, A. Boudard, S. Czajkowski, R. Legrain, S. Leray, B. Mustapha, M. Pravikoff, F. Rejmund, K.-H. Schmidt, C. Stéphan, J. Taïeb, L. Tassan-Got, and C. Volant, Nucl. Phys. **A686**, 481 (2001).
- [17] T. Enqvist, P. Armbruster, J. Benlliure, M. Bernas, A. Boudard, S. Czajkowski, R. Legrain, S. Leray, B. Mustapha, M. Pravikoff, F. Rejmund, K.-H. Schmidt, C. Stéphan, J. Taïeb, L. Tassan-Got, F. Vivès, C. Volant, and W. Wlazlo, Nucl. Phys. **A703**, 435 (2002).
- [18] J. Taïeb, K.-H. Schmidt, L. Tassan-Got, P. Armbruster, J. Benlliure, M. Bernas, A. Boudard, E. Casarejos, S. Czajkowski, T. Enqvist, R. Legrain, S. Leray, B. Mustapha, M. Pravikoff, F. Rejmund, C. Stéphan, C. Volant, and W. Wlazlo, Nucl. Phys. **A724**, 213 (2003).
- [19] M. Bernas, P. Armbruster, J. Benlliure, A. Boudard, E. Casarejos, S. Czajkowski, T. Enqvist, R. Legrain, S. Leray, B. Mustapha, P. Napolitani, J. Pereira, F. Rejmund, M. V. Ricciardi, K.-H. Schmidt, C. Stéphan, J. Taïeb, L. Tassan-Got, C. Volant, and W. Wlazlo, Nucl. Phys. **A725**, 213 (2003).
- [20] P. Armbruster, J. Benlliure, M. Bernas, A. Boudard, E. Casarejos, S. Czajkowski, T. Enqvist, S. Leray, P. Napolitani, J. Pereira, F. Rejmund, M.-V. Ricciardi, K.-H. Schmidt, C. Stéphan, J. Taïeb, L. Tassan-Got, and C. Volant, Phys. Rev. Lett. **93**, 212701 (2004).
- [21] C. Villagrasa, A. Boudard, J. E. Ducret, B. Fernández-Rodríguez, S. Leray, C. Volant, W. Wlazlo, P. Armbruster, T. Enqvist, F. Hammache, K. Helariutta, B. Jurado, M. V. Ricciardi, K.-H. Schmidt, K. Sümmerer, F. Vives, O. Yordanov, L. Audouin, L. Ferran, F. Rejmund, C. Stéphan, L. Tassan-Got, J. Benlliure, E. Casarejos, M. Fernández, J. Pereira, S. Czajkowski, D. Karamanis, M. Pravikoff, J. George, R. A. Mewaldt, N. Yanazak, A. Wiedenbeck, J. Connel, T. Faestermann, A. Heinz, and A. Junghans, AIP Conference Proceedings **769**, 842 (2005).
- [22] B. Fernández-Rodríguez, P. Armbruster, L. Audouin, J. Benlliure, M. Bernas, A. Boudard, E. Casarejos, S. Czajkowski, J. E. Ducret, T. Enqvist, B. Jurado, R. Legrain, S. Leray, B. Mustapha, J. Pereira, M. Pravikoff, F. Rejmund, M. V. Ricciardi, K.-H. Schmidt, C. Stéphan, J. Taïeb, and L. Tassan-Got, and C. Volant, Nucl. Phys. **A747**, 227 (2005).
- [23] M. Bernas, P. Armbruster, J. Benlliure, A. Boudard, E. Casarejos, S. Czajkowski, T. Enqvist, R. Legrain, S. Leray, B. Mustapha, P. Napolitani, J. Pereira, F. Rejmund, M. V. Ricciardi, K.-H. Schmidt, C. Stéphan, J. Taïeb, L. Tassan-Got, C. Volant, and W. Wlazlo, Nucl. Phys. **A765**, 197 (2006).
- [24] M. V. Ricciardi, P. Armbruster, J. Benlliure, M. Bernas, A. Boudard, S. Czajkowski, T. Enqvist, A. Kelić, S. Leray, R. Legrain, B. Mustapha, J. Pereira, F. Rejmund, K.-H. Schmidt, C. Stéphan, L. Tassan-Got, C. Volant, and O. Yordanov, Phys. Rev. C **73**, 014607 (2006).
- [25] C. Rubbia, J. A. Rubio, S. Buono, F. Carminati, N. Fiétier, J. Galvez, C. Gelés, Y. Kadi, R. Klapisch, P. Mandrillon, J. P. Revol, and Ch. Roche, Rep. CERN-AT/95-44(ET) (1995).
- [26] C. D. Bowman, Annu. Rev. Nucl. Part. Sci. **48**, 505 (1998).
- [27] <http://www.gsi.de>
- [28] M. Steiner, M. Blasche, H.-G. Clerc, H. Eickhoff, B. Franczak, H. Geissel, G. Münzenberg, K.-H. Schmidt, H. Stelzer, and K. Sümmerer, Nucl. Instrum. Methods A **312**, 420 (1992).
- [29] <http://www-aix.gsi.de/accelerator/sis.p14.html>
- [30] R. Anne, A. Lefol, G. Milleret, and R. Perret, Nucl. Instrum. Methods **152**, 395 (1985).
- [31] B. Jurado, K.-H. Schmidt, and K.-H. Behr, Nucl. Instrum. Methods A **478**, 493 (2002).
- [32] Ph. Chesny, A. Forgeas, J. M. Gheller, G. Guiller, P. Pariset, L. Tassan-Got, P. Armbruster, K.-H. Behr, J. Benlliure, K. Burkard, A. Brünle, T. Enqvist, F. Farget, and K.-H. Schmidt, GSI-reports LNS/SSGD/93-73.
- [33] H. Geissel, P. Armbruster, K. H. Behr, A. Brünle, K. Burkard, M. Chen, H. Folger, B. Franczak, H. Keller, O. Klepper, B. Langenbeck, F. Nickel, E. Pfeng, M. Pfützner, E. Roeckl,

- K. Rykaczewski, I. Schall, D. Schardt, C. Scheidenberger, K.-H. Schmidt, A. Schröter, T. Schwab, K. Sümmerer, M. Weber, G. Münzenberg, T. Brohm, H.-G. Clerc, M. Fauerbach, J.-J. Gaimard, A. Grewe, E. Hanelt, B. Knödler, M. Steiner, B. Voss, J. Weckenmann, C. Ziegler, A. Magel, H. Wollnik, J. P. Dufour, Y. Fujita, D. J. Vieira, and B. Sherrill, *Nucl. Instrum. Methods B* **70**, 286 (1992).
- [34] B. Voss, T. Brohm, H.-G. Clerc, A. Grewe, E. Hanelt, A. Heinz, M. de Jong, A. Junhans, W. Morawek, C. Röhl, S. Steinhäuser, C. Ziegler, K.-H. Schmidt, K.-H. Behr, H. Geissel, G. Münzenberg, F. Nickel, C. Scheidenberger, K. Sümmerer, A. Magel, and M. Pfützner, *Nucl. Instrum. Methods A* **364**, 150 (1995).
- [35] M. Pfützner, H. Geissel, G. Münzenberg, F. Nickel, C. Scheidenberger, K.-H. Schmidt, K. Sümmerer, T. Brohm, B. Voss, and H. Bichsel, *Nucl. Instrum. Methods B* **86**, 213 (1994).
- [36] H. Stelzer, *Nucl. Instrum. Methods A* **310**, 103 (1991).
- [37] J. Benlliure, J. Pereira, and K.-H. Schmidt, *Nucl. Instrum. Methods A* **478**, 493 (2002).
- [38] J. Pereira, J. Benlliure, and K.-H. Schmidt, *Nucl. Instrum. Methods B* **204**, 517 (2003).
- [39] J.-P. Dufour, H. Delangrange, R. Del Moral, A. Fleury, F. Hubert, Y. Llabador, M. B. Mauhourt, K.-H. Schmidt, A. Lleres, *Nucl. Phys.* **A387**, 157c (1982).
- [40] P. Karol, *Phys. Rev. C* **11**, 4, 1203 (1975).
- [41] T. Brohm and K.-H. Schmidt, *Nucl. Phys.* **A569**, 821 (1994).
- [42] J.-J. Gaimard and K.-H. Schmidt, *Nucl. Phys.* **A531**, 709 (1991).
- [43] P. Napolitani, L. Tassan-Got, P. Armbruster, and M. Bernas, *Nucl. Phys.* **A727**, 120 (2003).
- [44] T. Enqvist, J. Benlliure, F. Farget, K.-H. Schmidt, P. Armbruster, M. Bernas, L. Tassan-Got, A. Boudard, R. Legrain, C. Volant, C. Böckstiegel, M. de Jong, and J. P. Dufour, *Nucl. Phys.* **A658**, 47 (1999).
- [45] C. Scheidenberger, Th. Stöhlker, W. E. Meyerhof, H. Geissel, P. H. Mokler, and B. Blank, *Nucl. Instrum. Methods B* **142**, 441 (1998).
- [46] The GLOBAL program is available via anonymous ftp from borsu8.in2p3.fr in the directory */pub/nex/global/pc* and */pub/nex/global/vms_nix* for PCs and workstations, respectively.
- [47] R. Serber, *Phys. Rev.* **72**, 1114 (1947).
- [48] J. Benlliure, A. Grewe, M. de Jong, K.-H. Schmidt, and S. Zhdanov, *Nucl. Phys.* **A628**, 458 (1998).
- [49] B. D. Wilkins, E. P. Steinberg, and R. R. Chasman., *Phys. Rev. C* **14**, 1832 (1976).
- [50] U. Brosa, S. Grossmann, and A. Müller, *Phys. Rep.* **197**, 4, 167 (1990).
- [51] J. Pereira, A. Armbruster, J. Benlliure, and K.-H. Schmidt, submitted to *Phys. Rev. C*.
- [52] The EXFOR entries are available at the OECD NEA Data Bank, <http://www.nea.fr/html/dbdata>
- [53] P. C. Stevenson, H. G. Hicks, W. E. Nervi, and D. R. Nethaway, *Phys. Rev.* **111**, 886 (1958).
- [54] A. V. Prokofiev, *Nucl. Instrum. Methods A* **463**, 557 (2001).
- [55] H. de Vries, W. de Jager, and C. de Vries, *At. Data Nucl. Data Tables* **36**, 495 (1987).